EBioMedicine 48 (2019) 462–477

Contents lists available at ScienceDirect

EBioMedicine

journal homepage: www.elsevier.com/locate/ebiom

EBioMedicine
Published by THE LANCET

Research paper

Paracrine-endocrine FGF chimeras as potent therapeutics for metabolic diseases

Longwei Zhao[a,b,#], Jianlou Niu[a,#], Huan Lin[a], Jing Zhao[a], Yang Liu[c], Zihui Song[d], Congshang Xiang[d], Xiaojie Wang[a], Yong Yang[b], Xiaokun Li[a,*], Moosa Mohammadi[c,*], Zhifeng Huang[a,*]

[a] School of Pharmaceutical Sciences & Center for Structural Biology, Wenzhou Medical University, Wenzhou, Zhejiang 325035, China
[b] School of Life Science and Technology, China Pharmaceutical University, Nanjing 210009, China
[c] Department of Biochemistry & Molecular Pharmacology, New York University School of Medicine, New York, NY 10016, United States
[d] Tianjin Institute of Pharmaceutical Research, Tianjin 300301, China

ARTICLE INFO

Article history:
Received 26 August 2019
Revised 14 September 2019
Accepted 25 September 2019
Available online 17 October 2019

Keywords:
Fibroblast growth factor 21
Chimerisation
Thermal stability
Receptor binding affinity
Type 2 diabetes

ABSTRACT

Background: The development of a clinically useful fibroblast growth factor 21 (FGF21) hormone has been impeded by its inherent instability and weak FGF receptor (FGFR) binding affinity. There is an urgent need for innovative approaches to overcome these limitations.
Methods: We devised a structure-based chimerisation strategy in which we substituted the thermally labile and low receptor affinity core of FGF21 with an HS binding deficient endocrinised core derived from a stable and high receptor affinity paracrine FGF1 ($FGF1^{\Delta HBS}$). The thermal stability, receptor binding ability, heparan sulfate and βKlotho coreceptor dependency of the chimera were measured using a thermal shift assay, SPR, SEC-MALS and cell-based studies. The half-life, tissue distribution, glucose lowering activity and adipose tissue remodeling were analyzed in normal and diabetic mice and monkeys.
Findings: The melting temperature of the engineered chimera ($FGF1^{\Delta HBS}$-$FGF21^{C\text{-}tail}$) increased by ~22 °C relative to wild-type FGF21 ($FGF21^{WT}$), and resulted in a ~5-fold increase in half-life *in vivo*. The chimera also acquired an ability to bind the FGFR1c isoform – the principal receptor that mediates the metabolic actions of FGF21 – and consequently was dramatically more effective than $FGF21^{WT}$ in correcting hyperglycemia and in ameliorating insulin resistance in *db*/*db* mice. Our chimeric FGF21 also exerted a significant beneficial effect on glycemic control in spontaneous diabetic cynomolgus monkeys.
Interpretation: Our study describes a structure-based chimerisation approach that effectively mitigates both the intrinsically weak receptor binding affinities and short half-lives of endocrine FGFs, and advance the development of the FGF21 hormone into a potentially useful drug for Type 2 diabetes.

Research in context

Evidence before this study

The endocrine hormone fibroblast growth factor 21 (FGF21) is a potent modulator of glucose and lipid metabolism and a promising drug for type 2 diabetes, obesity and metabolic syndrome. However, the inherent instability and weak FGF receptor (FGFR) binding affinity are key features that have precluded its clinical application.

Added value of this study

Based on an in-depth understanding of the structure-function relationship of FGFs, we devised a chimerisation strategy in which we substituted the thermally labile and low receptor affinity core of an FGF hormone (FGF21) with an HS binding-deficient endocrinized core derived from a stable high receptor affinity paracrine FGF ($FGF1^{\Delta HBS}$). The chimeric FGF21 is metabolically more potent and longer acting than

* Corresponding authors.
E-mail addresses: lixk1964@163.com (X. Li), moosa.mohammadi@nyumc.org (M. Mohammadi), hzf@wmu.edu.com (Z. Huang).
# These authors contributed equally to this work.

https://doi.org/10.1016/j.ebiom.2019.09.052

native FGF21 in both mice and monkeys, and is therefore well poised to serve as the next generation of FGF21 agonists.

Implications of the available evidence

Our chimerisation strategy can readily be adapted to FGF19 and FGF23, thereby opening a new horizon for the discovery of rationally-designed and clinically effective agonists for all three endocrine FGFs. This approach thus has the potential to impart a major and lasting impact on the management of a wide spectrum of metabolic diseases for which there is a persistent unmet clinical need.

1. Introduction

FGF19, FGF21 and FGF23 together constitute a unique endocrine-acting subfamily within the structurally related FGF family of polypeptides, and function by regulating major metabolic axes in mammalian organisms [1,2]. FGF19 is secreted into the portal vein from the gut; upon reaching the liver and gallbladder, it regulates cholesterol catabolism and bile acid production [2–5]. FGF21 is a hepatokine which acts mainly on adipose tissue where it regulates glucose and lipid metabolism [6,7]. FGF21 may also signal in the central nervous system to increase energy expenditure and cause body weight loss [8–10]. FGF23 is secreted into the circulation by osteocytes, and signals in the kidney and parathyroid glands to maintain phosphate and vitamin D homeostasis [11–13]. Endocrine FGFs mediate their metabolic activities by binding, dimerizing and activating the alternatively spliced 'c' isoforms of the single-pass transmembrane FGF receptors 1–3 (FGFR1-3) and FGFR4.

Compared to paracrine-acting FGF family members, endocrine FGFs interact only weakly with heparan sulfate (HS) glycosaminoglycans, the O-linked sugar constituents of HS proteoglycans (HSPG) [14,15]. Consequently, these FGFs can freely permeate the HS-rich extracellular matrix, gain access to the circulation, and act in a hormonal fashion in distant organs [16,17]. In addition to having poor HS binding affinity, endocrine FGFs also interact weakly with their cognate FGFRs. As a result of these properties, HS alone is insufficient to mediate stable endocrine FGF-FGFR binding, dimerization and signalling. To offset this HS insufficiency, endocrine FGFs rely on Klotho proteins as additional co-receptors to bind, dimerize and activate their cognate receptors [18]. α- and βKlothos are single-pass transmembrane proteins whose extracellular portions consist of tandem TIM barrel domains (termed KL1 and KL2); these are structurally homologous to the TIM barrel domains found in β-glycosidases [19,20]. αKlotho serves as a co-receptor for FGF23 [21], whereas βKlotho is a co-receptor for both FGF19 and FGF21[22,23]. The Klotho dependency of endocrine FGFs also determines their target tissue specificities: αKlotho is predominantly expressed in the kidney and parathyroid glands [20,24,25], whereas βKlotho expression is highest in adipose tissue, liver, pancreas and the central nervous system (CNS) [26]. Notably, the restricted expression pattern of α/βKlotho co-receptors leads to the establishment of three important hormonal axes, namely gut-liver, liver-fat, and bone-kidney.

X-ray crystallographic studies of a ternary complex consisting of the naturally shed extracellular domain of αKlotho, the ectodomain of FGFR1c, and FGF23 - as well as of a binary complex of the extracellular domain of βKlotho with the C-terminal tail peptide of FGF21 - show that Klotho co-receptors serve as non-enzymatic molecular scaffolds in endocrine FGF signalling [27,28]. Klotho proteins simultaneously grip FGFR by its D3 domain and endocrine FGF by its long C-terminal tail, thereby enforcing endocrine FGF-FGFR proximity and conferring complex stability. Two such stabilized ternary complexes are then primed to unite into a symmetric 2:2:2 FGF-FGFR-Klotho quaternary dimer in the presence of two HS molecules, reminiscent of 2:2 paracrine FGF-FGFR dimers.

The discovery of FGF hormones as mediators of three major hormonal axes has spawned an intense effort to adopt these FGFs for the treatment of multiple metabolic diseases with an unmet clinical need, including diabetes, obesity, dyslipidemia, bile acid diarrhea, hypervitaminosis D and hyperphosphatemia [2,3,6,11,29]. Initial studies quickly established that native FGF hormones possess poor pharmacodynamic and kinetic properties arising from their intrinsically weak receptor binding affinities and short half-lives [2,17,30,31]. A range of standard methodologies - including non-specific and site-specific PEGylation, fusion with a humanized immunoglobulin Fc fragment, and site-directed mutagenesis – has been applied as a means to either mitigate their poor stability or enhance their efficacy [32–34]. More recently, alternative approaches have been attempted, including the application of mutagenesis-based optimization of the βKlotho binding site in the FGF21 C-tail and the generation of an agonistic anti-βKlotho monoclonal antibody that mimics FGF21 activity [35,36]. However, these efforts notwithstanding, as of today, no approved endocrine FGF-based drugs have been brought to market.

Here we describe a structure-based approach to advance the development of the FGF21 hormone into a clinically useful drug. Harnessing the known structure-function relationships of endocrine FGFs, we pinpointed the atypical β-trefoil core of endocrine FGFs as the root cause of their poor potencies and short half-lives *in vivo*. Based on this finding, and taking into consideration the recently established independent roles of the endocrine FGF core and the C-tail in endocrine FGF signalling [27], we devised a unique chimerisation approach. This method entailed replacing the thermally labile, low receptor binding affinity core of endocrine FGF with an endocrinised, thermally stable and high receptor binding affinity core region derived from paracrine FGFs. Endocrinisation of paracrine FGFs was accomplished by introducing structurally non-deleterious mutations into the HS binding site. The resulting chimera retains the authentic C-tail of endocrine FGFs, and thus preserves the tissue target selectivity of endocrine FGFs. We validated this approach by showing that a chimeric FGF21 (termed FGF1$^{\Delta HBS}$-FGF21$^{C\text{-}tail}$) consisting of an endocrinised FGF1 core and the C-terminal tail of FGF21 is metabolically more potent and longer acting than native FGF21 in mice and in monkeys. This technology opens up a new horizon for the discovery of rationally designed clinically effective endocrine FGF analogs, and could have a major and lasting impact on the management of metabolic diseases.

2. Materials and methods

2.1. Expression and purification of FGFs and the FGFR1c ectodomain

Full length human FGF1 (Met1-Asp155), its HS binding-defective derivative carrying a Lys127Asp/Lys128Gln/Lys133Val triple mutation (FGF1$^{\Delta HBS}$), full length human FGF2 (Met1-Ser155), mature human FGF4 (Ala67-Leu206) and human FGF9 (Asp35-Ser208) were expressed and purified according to published protocols [37,38]. N-terminally histidine-tagged, mature forms of human FGF19 (Arg23-Lys216), human FGF23 (Tyr25-Ile251) and the ligand-binding domain of human FGFR1c (Asp142-Arg365) were expressed in *E. coli* BL21 (DE3), refolded *in vitro* from bacterial inclusion bodies as previously described [31,38]. Wild-type mature human FGF21 (His29-Ser209) and its FGFR1c quintuple binding mutant (FGF21$^{K57S/L59E/K60S/P61V/Q65Y}$; FGF21^{mut}) were expressed using the p-SUMO-FGF21 or p-SUMO-FGF21^{mut} plasmid in

E. coli, and purified as described [32]. The FGF1$^{\Delta HBS}$-FGF21$^{C\text{-}tail}$ chimeric construct was engineered by PCR-based in-frame fusion of a DNA fragment encoding the Met1-Pro151 region using the expression construct for FGF1$^{\Delta HBS}$ and a cDNA fragment encoding the C-terminal tail of FGF21 (Gly169-Ser209) as templates. A βKlotho binding deficient variant of FGF1$^{\Delta HBS}$-FGF21$^{C\text{-}tail}$ (FGF1$^{\Delta HBS}$-FGF21$^{C\text{-}tail\Delta KLB}$) was generated by sequential introduction of Asp192Ala and Tyr207Ala mutations into its C-terminal tail. All mutations were engineered using the QuikChange site-directed mutagenesis kit (Agilent Technologies, Santa Clara, CA). Competent *E. coli* BL-21 (DE3) cells transformed with the FGF1$^{\Delta HBS}$-FGF21$^{C\text{-}tail}$ or FGF1$^{\Delta HBS}$-FGF21$^{C\text{-}tail\Delta KLB}$ expression construct were cultured in 1 L LB medium containing 2% glucose and 30 mg/mL kanamycin in an incubator shaker at 37 °C and 200 rpm. At an optical density of 0.8–1.0 at λ_{600}, recombinant protein expression was induced by addition of isopropyl-L-thio-β-D-galactopyranoside (IPTG) to 1 mM and further growth at 37 °C for 4 h. Cells were harvested and lysed in 25 mM HEPES (pH 7.5) buffer containing 150 mM NaCl, 10% glycerol and 0.5 mM phenylmethylsulfonyl fluoride (PMSF) using an Emulsiflex-C3 (Avestin, Inc., Ottawa, Canada) high volume homogenizer. The lysate was clarified by centrifugation at 20,000 rpm for 30 mins at 4 °C in an Avanti JA-25.5 centrifuge (Beckman Coulter, CA, USA), and the soluble recombinant protein purified by application to an anion exchange column (Source 15Q, GE Healthcare, Piscataway, NJ; column volume (CV) = 5 mL) equilibrated in buffer A (150 mM NaCl, 25 mM Tris-HCl, pH 8.0). The column was developed with a linear gradient of 1.0 M NaCl in buffer A. Fractions containing the protein of interest as determined by analysis via 12% SDS-PAGE were pooled, concentrated and applied to a gel filtration column (Superdex^{TM}-75 GE Healthcare, Piscataway, NJ) run in buffer C (1 M NaCl, 25 mM Tris–HCl, pH 8.0). The purity of the recombinant chimeric protein was estimated to be >98%.

2.2. SPR spectroscopy

All real-time biomolecular interactions were analyzed using a BIAcore T200 system (GE Healthcare, Piscataway, NJ) in HBS-EP buffer (10 mM HEPES-NaOH, pH 7.4, 150 mM NaCl, 3 mM EDTA and 0.005% (v/v) polylobate 20) at 25 °C. To determine HS-ligand binding affinities, biotinylated heparin (Sigma-Aldrich, St. Louis, MO) was immobilized onto flow channels of a research grade streptavidin chip (GE Healthcare, Piscataway, NJ). A dilution series of FGF1^{WT}, FGF21^{WT} and FGF1$^{\Delta HBS}$-FGF21$^{C\text{-}tail}$ was prepared in HBS-EP buffer and injected over the heparin chip for 180 s at a flowrate of 50 μL/min; HBS-EP buffer was then flowed at the same flow rate for 120 s to monitor dissociation. Sensor chips were regenerated by injecting 50 µL/min of 2.0 M NaCl in 10 mM sodium acetate, pH 4.5.

To measure interactions between βKlotho/FGFR1c and ligands, βKlotho and FGFR1c chips were prepared by covalent coupling of βKlotho or FGFR1c via their free amine groups onto flow channels of a CM5 sensor chip (GE Healthcare, Piscataway, NJ); the control flow channel was left blank. Increasing concentrations of FGF1^{WT}, FGF1$^{\Delta HBS}$, FGF21^{WT}, FGF1$^{\Delta HBS}$-FGF21$^{C\text{-}tail}$ and FGF1$^{\Delta HBS}$-FGF21$^{C\text{-}tail\Delta KLB}$ were prepared in HBS-EP buffer and injected over either a βKlotho chip for 120 s or a FGFR1c chip for 180 s at 50 μL/min; HBS-EP buffer was then flowed at the same rate for 120 s (or for 180 s in the case of the FGFR1c chip) to monitor dissociation. Sensor chips were regenerated as described above. Data were processed using BIA-Evaluation software; equilibrium dissociation constants (K_D) were calculated from fitted saturation binding curves.

2.3. HPLC-MALS analysis

An in-line HPLC (Waters 1525 Binary HPLC Pump equipped with a 2998 UV detector and a 717 plus auto-sampler)-MALS (Wyatt miniDawn-Treos and Optilab rEX) system was used to study complex assembly between FGF1^{WT} or FGF1$^{\Delta HBS}$-FGF21$^{C\text{-}tail}$ with the ligand-binding domain of FGFR1c in the presence of HS dodecasaccharide (MW=3 kDa). A Superdex^{TM} 200 10/300 GL gel filtration column (GE Healthcare, Piscataway, NJ) was equilibrated in 2×PBS by passing 5 column volumes of the buffer at a flow rate of 0.5 mL/min. Each experiment contained 60 μmoles of each component (FGF1^{WT}/ FGF1$^{\Delta HBS}$-FGF21$^{C\text{-}tail}$, FGFR1c and HS dodecasaccharide) at a final injection volume of 50 μL in 2xPBS. Light scattering and refractive index data were manually aligned to UV spectra using ASTRA software.

2.4. Fluorescence dye-based thermal shift assay

Thermal stability assays were done using a real-time PCR system (Bio-Rad, Hercules, CA) using a Protein Thermal Shift^{TM} Dye Kit (Thermal Fisher Scientific, MA, USA). 20 μL of various ligands (50 μM in 25 mM HEPES pH 7.5, 150 mM NaCl) were dispensed in duplicates in PCR strips. 5 μL dye was added by 200-fold dilution from a 5000-fold stock solution. A temperature gradient of 1 °C/min was applied in the range 4–95 °C. Fluorescence was recorded as a function of temperature in real time. Melting temperatures (T_m) were calculated with Step One software v2.2 as the maximum of the derivative of the resulting SYPRO Orange fluorescence curves.

2.5. Pharmacokinetic evaluation

In vivo half-lives of FGF21^{WT} and FGF1$^{\Delta HBS}$-FGF21$^{C\text{-}tail}$ were determined following intraperitoneal (i.p.) injection of a single dose (0.5 mg/kg in PBS) into adult male Sprague Dawley (SD) rats (220–250 g). Blood aliquots (200 μL) were drawn from the tail vein at various times over the course of 9 h, and specific protein levels were measured using human FGF21 and FGF1 immunoassay ELISA kits (R&D Systems, Minneapolis, MN). Pharmacokinetic parameters were calculated using the Drug and Statistics Software (DAS, v 2.0; Mathematical Pharmacology Professional Committee of China). Elimination half-lives ($t_{1/2}$) were calculated using the formula $t_{1/2} = 0.693/K_e$, where K_e is the elimination rate constant.

2.6. Mitogenicity assay

NIH 3T3 cells were grown to mid-logarithmic phase, transferred to a 96-well plate (5×10^3/well), starved for 24 h in DMEM without fetal bovine serum (FBS), and incubated with various concentrations of FGF1^{WT} or FGF1$^{\Delta HBS}$-FGF21$^{C\text{-}tail}$ for 48 h. The number of viable cells was determined using an MTT-based Cell Growth Determination Kit (Sigma-Aldrich, St. Louis, MO). For mitogenicity assays *in vivo*, male C57BL/6 J mice (2 months old) were injected intravenously with vehicle (PBS), FGF1^{WT} or FGF1$^{\Delta HBS}$-FGF21$^{C\text{-}tail}$ (2.0 mg/kg body weight) every day for 20 days. After treatment, mice were sacrificed and liver tissues were collected for immunohistochemical staining and western blot analyses.

2.7. Generation and stimulation of BaF3 cell lines

Murine pro-B BaF3 cell lines overexpressing wild-type FGFR1c were generated as described previously [38]. Briefly, BaF3 cells were infected with lentiviruses engineered to express the FGFR1c gene. After incubation for 2 days in RPMI 1640 medium containing 0.3 mg/L L-glutamine, 10% FBS, 50 nM beta-mercaptoethanol, 100 IU/mL penicillin, 100 mg/mL streptomycin sulfate, and 3 ng/mL

murine IL-3 (Thermo Fisher Scientific Waltham, MA) at 37 °C/5% CO_2, cells were selected for neomycin resistance to isolate clones stably expressing FGFR1c. Cells were starved for 5 h in FBS/IL-3 free RPMI 1640 medium followed by 10 min of stimulation with increasing concentrations (10, 50 and 100 ng/mL) of $FGF21^{WT}$ or $FGF1^{\Delta HBS}$-$FGF21^{C\text{-}tail}$. Heparin (final concentration, 5 μg/mL) was added to the culture medium before stimulating the cells with FGF ligands. BaF3 cell lines co-expressing FGFR1c and βKlotho were established by infecting the BaF3-FGFR1c cell line with lentivirus expressing the βKlotho gene. After infection, cell lines were selected in medium containing neomycin and hygromycin (0.1% v/v) for 10 days. Stimulation of selected cell lines was done as described above with $FGF21^{WT}$ or $FGF1^{\Delta HBS}$-$FGF21^{C\text{-}tail}$ as ligands.

2.8. Adipocyte cell-based experiments

3T3-L1 pre-adipocytes (3T3-L1 MBX ATCC® CRL-3242™) were cultured as described previously [6], and were seeded at a density of 150,000 cells/well in 1 mL culture medium in 6-well plates. Cells were differentiated to mature adipocytes by culturing for 2 days in differentiation medium [DMEM, high glucose/10% FBS/10 mM Hepes/MEM nonessential amino acids (NEAA)/penicillin/streptomycin (PC/SM) (the latter from Thermo Fisher Scientific Waltham, MA)/2 μM insulin/1 μM dexamethasone/0.5 mM 3-isobutyl-1-methylxanthine (IBMX) (the latter from Sigma–Aldrich, St. Louis, MO)] and then culturing in differentiation medium without dexamethasone and IBMX for a further 2 days. Thereafter, the medium was changed every 2 days with DMEM supplemented with 10% FBS/10 mM Hepes/NEAA/PC/SM. After 7 days, cells containing accumulated lipid droplets (>95%) were used for experiments. βKlotho dependence was assayed by stimulating pre-adipocytes and mature adipocytes with increasing concentrations (10, 50 and 100 ng/mL) of $FGF21^{WT}$ or $FGF1^{\Delta HBS}$-$FGF21^{C\text{-}tail}$ for 20 min. Cells were lysed and the levels of various downstream signals detected by western blotting (see western blotting methods).

2.9. Quantification of ERK phosphorylation

Pre-adipocytes or mature adipocytes were stimulated with various concentrations of $FGF21^{WT}$, $FGF1^{\Delta HBS}$-$FGF21^{C\text{-}tail}$ or $FGF1^{\Delta HBS}$-$FGF21^{C\text{-}tail\Delta KLB}$ (0, 0.001, 0.01, 0.1, 1, 10, 100 nM for each) for 20 min as described above. ERK phosphorylation levels of cell lysates were measured using Advanced phospho-ERK1/2 Thr202/Tyr204 kit-500 assay kits (Cat#64AERPEG, Cisbio Bioassays, France) using the protocols provided. Phosphorylated ERK values were normalized by dividing the value of the phosphor signal with the maximal signal obtained in response to $FGF1^{\Delta HBS}$-$FGF21^{C\text{-}tail}$ treatment. 95% confidence intervals (CI) were determined by a applying a 4-parameter logistic nonlinear regression analysis using GraphPad Prism version 7.0 (GraphPad Software, San Diego, California).

2.10. Western blot analysis

3T3-L1 adipocytes, NIH-3T3 cells, BaF3 cells or mouse tissues were lysed using RIPA lysis buffer (25 mM Tris, pH 7.6, 150 mM NaCl, 1%NP-40,1% sodium deoxycholate, 0.1% SDS) containing protease and phosphatase inhibitors (Thermo Fisher Scientific Waltham, MA), and total protein samples were quantified using a BCA Kit (Protein Assay Kit, Beyotime Biotechnology, Shanghai, China). 40 micrograms of total lysate proteins from cells or tissues were separated using 8–12% SDS-PAGE and electro-transferred onto a nitrocellulose membrane. Protein blots were probed with antibodies against phospho-FGFR1, FGFR1, phospho-ERK1/2, ERK1/2, Ki67, phospho-ACC, phospho-AKT, SCD-1, FAS, PPARγ, GAPDH (all from Cell Signalling Technology, Danvers, MA), CPT-1α (Novus Biologicals, Colorado, USA) or β-actin (Abcam, Cambridge, MA). Immuno-reactive bands were detected by incubating with secondary antibody (Santa Cruz Biotechnology, Dallas, TX) conjugated with horseradish peroxidase and visualized using enhanced chemiluminescence (ECL) reagents (Bio-Rad, Hercules, CA). Quantification of immuno-reactive proteins was analyzed using Image J software version 1.38e (NIH, Bethesda, MD) and normalized against their respective controls.

2.11. RNA extraction, cDNA synthesis and quantitative RT-PCR

Total RNA was extracted from mouse tissues with TRIzol reagent (Thermo Fisher Scientific, Waltham, MA) and reverse transcribed into complementary DNA with Prime Script RT reagent kit (Takara). Quantitative real-time PCR was done using SYBR Premix Ex Taq (Takara) with specific primers (listed in **Table S1**) on a StepOnePlus Real-Time PCR system (Applied Biosystems® QuantStudio® 3). β-actin was used as an endogenous control to normalize for differences in the amount of total RNA contained in each reaction.

2.12. Animals and animal welfare

2.12.1. Mice

Male C57BL/6 J mice, male *db/db* (C57BLKS/J-leprdb/leprdb) and their lean littermate control mice (*db/m*) were purchased from the Model Animal Research Center of Nanjing University, China. All protocols used in these studies were approved by the Animal Care and Use Committee of Wenzhou Medical University, China. Animals were housed in a specific pathogen-free (SPF) animal facility with a controlled environment (22±1 °C, 50–60% humidity, 12-hour light-dark cycle, lights on at 7 am) and free access to food and water.

2.12.2. Normal monkeys

Clinically healthy, socially housed adult cynomolgus monkeys (3–5 years old, 2.90–4.50 kg) were purchased from Xiang Guan Biotechnology Co. Ltd, GuangZhou, China. Monkeys were housed in a GLP facility certified by the Chinese FDA at the Safety Evaluation for Drugs Department at the Tianjin Pharmaceutical Research Institute, China. Animals were housed, acclimatized, maintained, and fed exactly as described by Talukdar et al., 2016[50]. All studies were conducted in accordance with current guidelines for animal welfare (Institute for Laboratory Animal Research [ILAR] Guide for the Care and Use of Laboratory Animals, 1996; Animal Welfare Act, 1966, as amended in 1970, 1976, and 1985, 9 CFR Parts 1, 2, and 3). Procedures were approved by the Institutional Animal Care and Use Committee of Tianjin Pharmaceutical Research Institute, China.

2.12.3. Diabetic monkeys

Chinese-origin middle-aged (10–16 years) cynomolgus monkeys with spontaneous diabetes mellitus (fasting blood glucose ≥6.0 mM) (4 males, mean body weight, 10±3 kg, and 2 females, mean body weight, 5 ± 2 kg) were purchased from Xin Gui Biotechnology Co. Ltd, Guangxi, China. These animals were housed and treated as previously described [50]. All procedures involving diabetic monkeys were approved by the Institutional Animal Care and Use Committee of GuangXi, China.

2.13. Drug biodistribution

$FGF21^{WT}$, $FGF1^{\Delta HBS}$-$FGF21^{C\text{-}tail}$, $FGF1^{\Delta HBS}$ and $FGF1^{\Delta HBS}$-$FGF21^{C\text{-}tail\Delta KLB}$ were labeled with Alexa Fluor 647 fluorescent dyes following the manufacturer's instructions (Alexa Fluor® 647 Protein Labeling Kit, A30009) and were administered intraperitoneally

at a dose of 0.5 mg/kg to overnight-fasted C57BL/6 J mice (22–25 g). At specific time intervals (0 min, 15 min, 30 min), mice were anesthetized by injection with 80 mg/kg pentobarbital sodium and fluorescence distribution was determined using a small animal *in vivo* imaging instrument (Vilber NEWTON 7.0, France). Filter sets (blue: excitation, 500–720 nm; exposure time, 200 ms; red: excitation, 640–700 nm; exposure time, 150 ms) were used to detect fluorescence. At 30 min post-administration, multiple organs (epididymal fat, liver, pancreas, muscle, kidney, heart, lung, spleen, and stomach) were excised for further observation using the same imaging instrument.

2.14. Evaluation of βKlotho dependent function of $FGF1^{\Delta HBS}$-$FGF21^{C\text{-}tail}$ in vivo

Male C57BL/6 J mice (2 months old) were injected subcutaneously with vehicle (PBS), $FGF1^{\Delta HBS}$, $FGF21^{WT}$or $FGF1^{\Delta HBS}$-$FGF21^{C\text{-}tail}$ at a dose of 0.5 mg/kg body weight. After 30 min, epididymal fat, liver, pancreas, heart, kidney, spleen, lung, muscle, small intestine, and stomach were harvested, homogenized and lysed using the proprietary T-PER Tissue Protein Extraction Reagent supplemented with protease and phosphatase inhibitors (Thermo Fisher Scientific Waltham, MA). Lysates were analyzed for the presence of ERK phosphorylation by western blotting as readout for FGF signalling.

2.15. Functional evaluation of $FGF1^{\Delta HBS}$-$FGF21^{C\text{-}tail}$ in db/db mice

Before each study, body weight was measured and whole-blood glucose was determined in samples taken from the tail vein using a Free Style complete blood glucose monitor (Abbott Diabetes Care Inc., Alameda, CA). 18 *db/db* mice were randomized (based on their glucose levels and body weights) and placed into 3 groups of 6 mice each: a control, $FGF21^{WT}$, and an $FGF1^{\Delta HBS}$-$FGF21^{C\text{-}tail}$ group. The control group was treated with vehicle (PBS), while the other two groups received either $FGF21^{WT}$ or $FGF1^{\Delta HBS}$-$FGF21^{C\text{-}tail}$ (see below). *db/m* mice were treated with PBS as an additional control.

For acute dose-response and time-course studies, blood samples were taken from conscious, fed *db/m* or *db/db* animals by tail snip at the indicated time-points (see Fig. 5) after a single intraperitoneal injection of $FGF21^{WT}$, $FGF1^{\Delta HBS}$-$FGF21^{C\text{-}tail}$ (0.125 mg/kg or 0.5 mg/kg body weight) or buffer alone. Blood glucose levels were measured as described above. For chronic efficacy evaluation, mice were subcutaneously injected with $FGF21^{WT}$ and $FGF1^{\Delta HBS}$-$FGF21^{C\text{-}tail}$ at a daily dose of 0.5 mg/kg body weight for 24 successive days with buffer (PBS) and insulin (10 IU/kg, Humulin R, Eli Lilly, Indianapolis, IN) as controls. Following the final dose, glucose tolerance tests (GTT) were conducted after fasting overnight (12 h): mice were challenged with a glucose solution (2 g/kg body weight, IP), and blood was collected at 0, 15, 30, 60 and 120 min post-injection; glucose levels were determined as described above. Area under the curve (AUC) was calculated by the trapezoid rule for the glucose tolerance curve using GraphPad Prism 7.0 software. NEFA (Non-Esterified Fatty Acid, Antibodies-online, Germany), GSP (Glycosylated Serum Protein, Antibodies-online, Germany); Serum Insulin (Merck Millipore, Germany), C-peptide (Connecting Peptide, Merck Millipore, Germany), were measured using corresponding enzyme-linked immunosorbent assay (ELISA) kits following the manufacturer's instructions.

2.16. Indirect calorimetry

db/db mice were acclimated for 24 h in metabolic cages prior to treatment with $FGF1^{\Delta HBS}$-$FGF21^{C\text{-}tail}$ (0.5 mg/kg body weight) daily for 24 successive days; PBS was used as a control. Light and dark cycle measurements of all animals were recorded for two complete days at 49-minute intervals. Oxygen consumption (VO2), carbon dioxide production (VCO2), respiratory exchange ratio (RER) and ambulatory activity were measured using an indirect calorimetry system (Oxymax, Columbus Instruments, Columbus, OH).

2.17. Pathological, histopathological and immunohistochemical and immunofluorescent evaluation

Six mice were used per group. Livers, epididymal white adipose tissues (Epi-WAT), subcutaneous adipose tissues and brown adipose tissues (BAT) were excised from *db/m* (control) and *db/db* animals 24 days following chronic administration of either PBS (as a control), $FGF1^{\Delta HBS}$-$FGF21^{C\text{-}tail}$ or $FGF21^{WT}$ (the latter two at 0.5 mg/kg body weight) and weighed. Tissues were fixed overnight in 4% paraformaldehyde and embedded in either paraffin or Tissue-Tek OCT compound (Sakura, Tokyo, Japan). After deparaffinization and rehydration, paraffin sections (5 μm) were stained with hematoxylin and eosin (H&E) reagent using standard procedures. For immunofluorescence, paraffin sections of Epi-WAT were incubated overnight at 4 °C with primary antibody (anti-glucose transporter GLUT1 antibody (1:200), from Abcam, Cambridge, MA). After washing, sections were incubated with a donkey anti-mouse IgG H&L (Alexa Fluor® 488) secondary antibody (1:1000 dilution) (Abcam, Cambridge, UK) at room temperature for 1 h followed by a 10 min incubation with 4′,6-diamidino-2-phenylindole (DAPI) (Southern Biotech, Birmingham, AL).

Liver steatosis was visualized by Oil red O staining of liver cryosections. For immunocytochemistry, paraffin sections were incubated with primary antibody [rabbit polyclonal to Ki67 (1:500), Abcam Cambridge, MA] overnight at 4 °C. After washing, sections were incubated with horseradish peroxidase-conjugated anti-rabbit secondary antibody, developed with a DAB (3,3-diaminobenzidine) developing system (Beyotime Biotechnology, Shanghai, China), and counterstained with hematoxylin. To determine triglyceride (TG), alanine aminotransferase (ALT) and aspartate aminotransferase (AST) levels, 100–200 mg of liver tissues were extracted using a chloroform/methanol mixture (2:1 v/v). Hepatic extracts were lyophilized in a stream of nitrogen gas and dissolved in 5% fatty acid-free BSA. Resuspended extracts were used for measurements of TG, ALT and AST using a VET Test Chemistry Analyzer according to the manufacturer's instructions (Antibodies-online, Germany).

2.18. Effect of $FGF1^{\Delta HBS}$-$FGF21^{C\text{-}tail}$, $FGF21^{WT}$ and $FGF1^{\delta HBS}$ on food intake and body weight in cynomolgus monkeys

Four groups of clinically healthy monkeys, each comprising one male and one female per group, were used. One group received 0.9% NaCl saline solution, while the other three groups were given $FGF1^{\Delta HBS}$-$FGF21^{C\text{-}tail}$, $FGF21^{WT}$ or $FGF1^{\Delta HBS}$ by daily subcutaneous administration at a dose of 1.5 mg/kg (this dose is a 10-fold effective dose based on weight comparison between mice and monkeys). Food consumption was noted at the indicated time and body weight was measured on day zero, D8, D18 and D28.

2.19. Effect of $FGF1^{\Delta HBS}$-$FGF21^{C\text{-}tail}$ on metabolic regulation in spontaneous cynomologous monkeys with T2D

After a 60-day acclimatization period, 6 diabetic cynomolgus monkeys (4 male, 2 female) were randomized into two groups (control and experimental) based on their gender, age, body weight (BW), fasting blood glucose and body mass index (BMI) (2 male and 1 female per group). In the experimental group, $FGF1^{\Delta HBS}$-$FGF21^{C\text{-}tail}$ (0.05 or 0.15 mg/kg of body weight, termed as low dose and high dose, respectively) contained in 0.9% NaCl saline solution (0.5 mL/kg of body weight) was administered daily subcuta-

neously at about 9:30 am for 15 days at low dose followed by an additional 15 days at high dose. Control diabetic monkeys received saline solution subcutaneously (0.5 mL/kg) once a day for 30 days. Fasting glucose was detected via a blood glucose meter at approximately 8:30 am on day 0, 6, 8, 10, 14, 16, 20, 24 and 28. 2.5 mL of blood was collected from the post-femoral vein of each monkey at approximately 9:00 am on day 0, 14 and 29 for HbAIc and plasma lipid measurement. For OGTT evaluation, monkeys were fasted overnight (12 h) and challenged with an oral glucose solution (4 g/8 mL/kg body weight). Blood was collected at 0, 15, 30, 60, 90, 120 and 180 min post-administration, and glucose and insulin levels determined as described above. Food consumption was noted twice per day (at approximately 9:00 am and 4:00 pm) and body weight was measured at approximately 9:30 am on day zero, D6, D14, D20 and D28.

2.20. Statistical analysis

All *in vitro* experiments were repeated in triplicate. All data were expressed as the mean ± SEM and subjected to statistical analysis by one-way or two-way ANOVA and a Student *t*-test using statistical software NASDAQ: SPSS from SPSS Inc. A p value of <0.05 was considered to be statistically significant.

3. Results

3.1. Atypical β-trefoil cores of endocrine FGFs impart short half-lives and weak receptor binding affinities

Structural comparison of endocrine and paracrine FGFs shows that endocrine FGFs adopt atypical and less compact β-trefoil folds (**Fig. 1a–c**). This is due to unusual conformations in the stretch between β strands 10 and 12, a segment which houses a major HS binding site in paracrine FGFs [17]. Notably, endocrine FGFs lack a β-strand that corresponds to the β11 strand in this region of paracrine FGFs (**Fig. 1b**). This structural divergence reflects the absence of sequence homology within this region between endocrine and paracrine FGFs: the region between β10 and β12 strands in FGF hormones is not only shorter, but also lacks the GXXXXGXX (T/S) sequence motif conserved in all paracrine FGFs (**Fig. 1a–c**) [17,39]. The latter motif plays an important role in shaping the uniform conformation of the stretch between β10 and β12 strands across paracrine FGFs, and accounts for their canonical closed-off and rigid β-trefoil core. The conserved conformation of this stretch is critical for the formation of hydrogen bonds between the backbone and side chains in this region and sulfate moieties in HS [17,30]. In contrast, the altered conformation of the same region in FGF hormones is incompatible with the formation of such hydrogen bonds. This results in a major loss of HS binding affinity, and forms the basis of the endocrine behavior of these ligands. An additional and important functional consequence of the distinctive conformations of the stretch between β10 and β12 strands in endocrine FGFs is that their core is not fully closed off, and is thus less compact [17,40]. This feature would be expected to render endocrine FGFs structurally and thermally more labile, potentially accounting for their short half-lives *in vivo*. Guided by these structural considerations, we compared the thermal stabilities of endocrine and paracrine FGFs using a fluorescence dye-based thermal shift assay. In agreement with our structural predictions, these experiments showed that all three FGF hormones have lower melting temperatures (T_m) compared to the four paracrine ligands tested, namely FGF1, FGF2, FGF4 and FGF9 (**Fig. 1d**).

In contrast to paracrine FGFs, the binding of FGF hormones to their cognate FGFRs is either very weak (FGF19 and FGF23) or undetectable (FGF21) [23,30,31,40–42]. Based on the crystal structure of the FGF1-FGFR1c complex (**Fig. 1e**), FGF21's weak receptor binding affinity stems primarily from a reduced ability of its core region to interact with the receptor D3 domain. Notably, replacement of residues S62, E64, S65, V66 and Y70 from the β4-β5 strand pair region of FGF1 with the corresponding residues in FGF21 (namely K57, L59, K60, P61 and Q65) would be expected to disrupt numerous hydrogen bonding and hydrophobic contacts with the βC'-βE loop in the D3 domain of FGFR1c (**Fig. 1f,g**). To test this notion, we mutated all five of these residues in FGF21 to the corresponding residues in FGF1, and tested the ability of the resulting mutant protein ($FGF21^{mut}$) to bind FGFR1c using surface plasmon resonance (SPR) spectroscopy. $FGF1^{WT}$ bound FGFR1c with a K_d of 273 nM (**Fig. 1h**). However, in accord with previously published data [30,31,42], $FGF21^{WT}$ did not bind to FGFR1c at all (**Fig. 1i**). In contrast, $FGF21^{mut}$ acquired significant affinity for FGFR1c (**Fig. 1j**), but it retained the same poor stability as $FGF21^{WT}$ (**Supplementary Fig. 1a**). These data are fully consistent with our structure-based predictions. We conclude that the atypical cores of FGF hormones account for both their structural/thermal instability and their weak FGFR binding affinity.

3.2. Stability of paracrine/endocrine chimeras in vitro and in vivo

With these data in hand, we reasoned that stabilized, high affinity analogs of endocrine FGFs could be engineered by replacing their thermally atypical labile core with a structurally more rigid, high affinity canonical core derived from a paracrine FGF. This paracrine-endocrine chimerisation approach seemed particularly promising in light of our recently determined structure of the FGF23-FGFR1c-αKlotho ternary complex (PDB ID: 5W21) [27]. The structure shows that the core domain and C-tail of endocrine FGF fulfill functionally independent roles in endocrine FGF signalling [27]. Specifically, the core region of endocrine FGF engages FGFR in much the same manner as paracrine FGFs, while the unique C-tail of endocrine FGF latches onto Klotho co-receptors (**Fig. 2a**).

We chose FGF21 to examine the feasibility of our approach because among endocrine FGFs, it is the least stable (**Fig. 1c**) and also lacks virtually all receptor binding ability [30,31,40,43]. We replaced the labile atypical core of FGF21 with the thermally more stable, high affinity β-trefoil core of paracrine FGF1 carrying three mutations (i.e., Lys127Asp, Lys128Gln and Lys133Val) in its HS binding site (termed $FGF1^{\Delta HBS}$) resulting in a $FGF1^{\Delta HBS}$-$FGF21^{C\text{-}tail}$ chimera containing the authentic C-terminal tail of FGF21 (Gly169-Ser209) that mediates binding to βKlotho (**Fig. 2b**). We previously showed that $FGF1^{\Delta HBS}$ has a dramatically reduced HS binding affinity [37], enabling it to behave in an endocrine fashion while possessing an enhanced thermal stability compared to $FGF1^{WT}$ (**Supplementary Fig. 1b**). Consistent with our previous data on $FGF1^{\Delta HBS}$ [37], SPR analysis showed that the chimera has negligible HS binding ability (**Fig. 2c**). SPR analysis also showed that the chimera is indistinguishable from $FGF21^{WT}$ in terms of binding to the soluble βKlotho ectodomain, whereas $FGF1^{\Delta HBS}$ lacked any measurable binding affinity (**Fig. 2d–f**).

We next compared the *in vitro* thermal stabilities of the $FGF1^{\Delta HBS}$-$FGF21^{C\text{-}tail}$ chimera and $FGF21^{WT}$, and found that the T_m of the chimera was ~22 °C higher compared to $FGF21^{WT}$ (**Fig. 2g**). To see whether this enhanced thermal stability confers a longer half-life *in vivo*, we compared the pharmacokinetics of $FGF1^{\Delta HBS}$-$FGF21^{C\text{-}tail}$, $FGF21^{WT}$ and $FGF1^{WT}$ following single injections of these proteins into Sprague Dawley (SD) rats. As shown in **Fig. 2h,i** and **Table S2**, the half-life of $FGF1^{\Delta HBS}$-$FGF21^{C\text{-}tail}$ (~1.99 h) was nearly 5 times longer than in the case of $FGF21^{WT}$ (~0.43 h) ($p<0.001$, unpaired *t*-test). As expected, the half-life of $FGF1^{\Delta HBS}$-$FGF21^{C\text{-}tail}$ was comparable to that of $FGF1^{WT}$ (~2.0 h) (**Supplementary Fig. 1c, d**). We also found that the $FGF1^{\Delta HBS}$-$FGF21^{C\text{-}tail}$ chimera was able to bind FGFR1c with an affinity similar to that of $FGF1^{WT}$ (**Fig. 2j and 1h**). Taken together, these data unequivocally

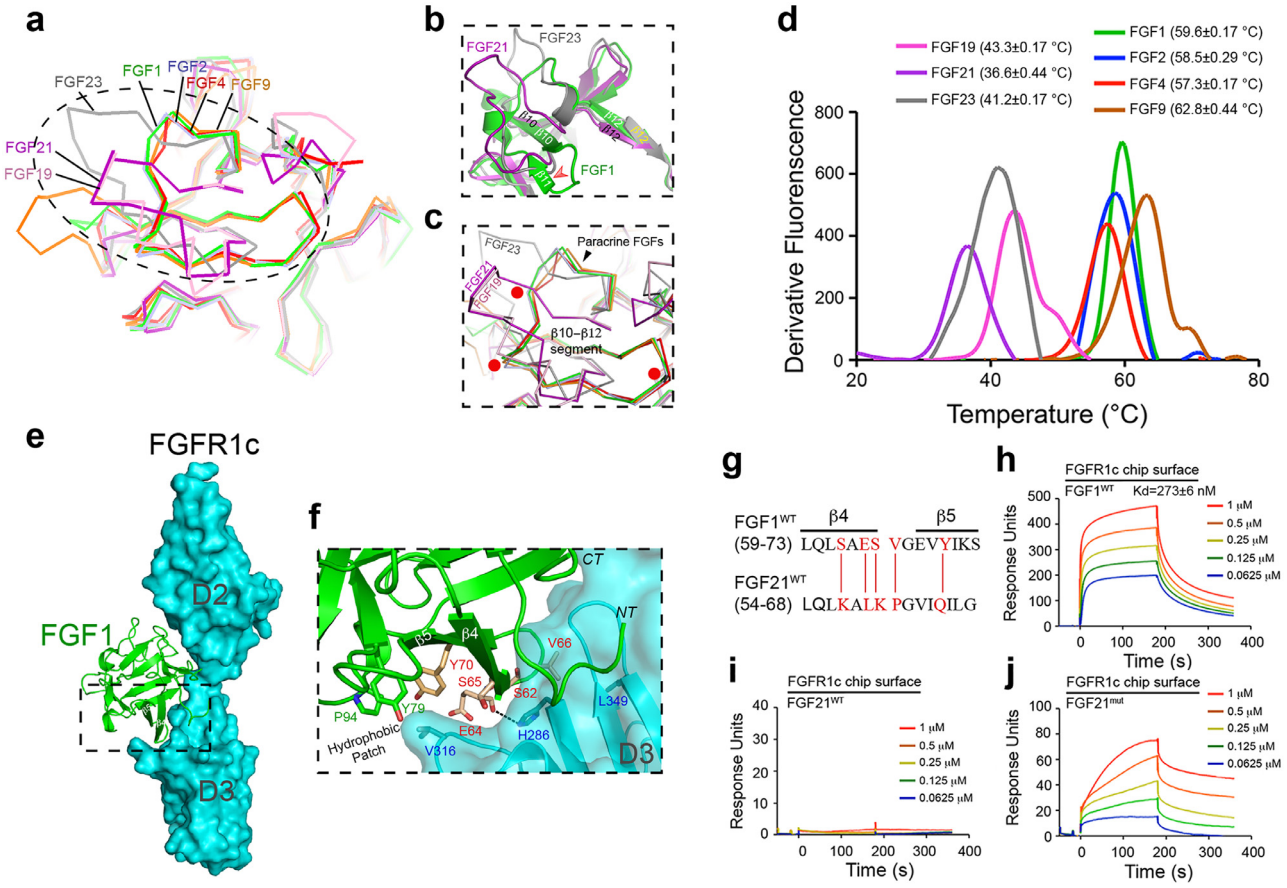

Fig. 1. . **The atypical trefoil core domain of endocrine FGFs imparts thermal instability and a weak receptor binding affinity**
(a) Structural comparison of paracrine and endocrine FGFs highlighting major differences in their HS binding domains. The view is from the top looking down onto the β-trefoil core. An overlay of Cα traces of four paracrine FGFs [FGF1 (PDB: 2AFG), FGF2 (PDB: 4OEE), FGF4 (PDB: 1IJT), FGF9 (PDB: 1IHK)] and three endocrine FGFs [FGF19 (PDB: 2P23), FGF23 (PDB: 2P39)] is shown. For FGF21, a homology model was used because an experimentally derived crystal structure is lacking. The FGF21 model was generated using an automated SWISS-MODEL homology-modeling pipeline (www. swissmodel. expasy. org) on the basis of the structure of its subfamily member FGF19 (PDB: 2P23). **(b)** Close-up view of the major HS binding site between β10 and β12 strands of FGF1 (used as a representative of paracrine FGFs) and FGF21 or FGF23. Note that endocrine FGFs do not have an equivalent β11 strand and are therefore atypical. **(c)** Superimposition of the atypical β-trefoil core of endocrine FGFs (FGF19/FGF21/FGF23) onto the canonical β-trefoil core of FGF1/FGF2/FGF4/FGF9. Locations of glycine and threonine residues of the GXXXXGXX (T/S) motif conserved only in paracrine ligands (FGF1, FGF2, FGF4 and FGF9) are highlighted by red dots. In a-c, FGF19, FGF21, FGF23, FGF1, FGF2, FGF4 and FGF9 are indicated in pink, purple, gray, green, light blue, red and orange, respectively. **(d)** Comparison of melting temperatures (T_m) of paracrine FGFs (FGF1/FGF2/FGF4/FGF9) and endocrine FGFs (FGF19/FGF21/FGF23) obtained by a fluorescence dye-based thermal shift assay. T_m values from three independent measurements are presented as mean ± SEM. **(e)** Crystal structure of FGF1-FGFR1c (PDB: 3OJV). FGFR1c (comprising D2 and D3 domains) and FGF1 are represented as a cyan molecular surface and a green cartoon, respectively. **(f)** An expanded view of the region boxed in (E) showing contacts between the hydrophobic patch of FGF1 and the D3 domain of FGFR1c. Selected residues in FGF1 (S62/E64/S65/V66/Y70/Y79/P94, labeled in red or green) and the FGFR1 D3 domain (labeled in blue) are represented as sticks. The β4 and β5 strands of FGF1 are labeled. Note that FGF1 residues labeled in red are not conserved between FGF21 and FGF1 (see panel g). A hydrogen bond between E64 in FGF1 and H286 in FGFR1 is depicted as a dashed line. Oxygen and nitrogen atoms are shown in red and blue, respectively; *NT, CT* denote the location of the FGF1 N- and C-termini. **(g)** Structure-based sequence alignment of $FGF1^{WT}$ (aa 59–73) and $FGF21^{WT}$ (aa 54–68). Secondary structure elements are indicated on top of the sequence alignment. The five residues in $FGF21^{WT}$ that were mutated so as to correspond to those in $FGF1^{WT}$ (thus generating $FGF21^{mut}$) are highlighted in red. **(h-j)** Representative SPR sensorgrams of binding interactions between $FGF1^{WT}$ (h), $FGF21^{WT}$ (i) and $FGF21^{mut}$ (j) with FGFR1c. $FGF1^{WT}$, $FGF21^{WT}$ and $FGF21^{mut}$ at the indicated concentrations were passed over CM5 chips containing the immobilized FGFR1c ligand-binding domain. In (h), K_d values from three independent measurements are presented as mean ± SEM.(For interpretation of the references to colour in this figure legend, the reader is referred to the web version of this article.)

show that our paracrine-endocrine chimerisation approach can be applied to generate analogs of endocrine FGFs that have greater structural stability and enhanced FGFR binding affinity.

3.3. $FGF1^{\Delta HBS}$-$FGF21^{C\text{-}tail}$ signals weakly in an HS-dependent paracrine fashion

We next characterized the HS and βKlotho dependencies of the $FGF1^{\Delta HBS}$-$FGF21^{C\text{-}tail}$ chimera. In size exclusion chromatography/multi-angle light scattering (SEC-MALS) experiments, we found that the HS decasaccharide caused stoichiometric dimerization of the $FGF1^{WT}$-FGFR1c complex, with the molecular mass of the dimeric species (90.5 kDa) closely matching that of a 2:2:2 dimer (91.6 kDa) (**Fig. 3a**). In contrast, in the presence of HS, the $FGF1^{\Delta HBS}$-$FGF21^{C\text{-}tail}$-FGFR1c complex eluted as a 44 kDa species (**Fig. 3a**), demonstrating that the chimera is severely impaired in its ability to dimerize the FGFR1c ectodomain in an HS-dependent manner.

In agreement with these SEC-MALS data, NIH 3T3 cell-based experiments showed that $FGF1^{\Delta HBS}$-$FGF21^{C\text{-}tail}$ is almost two orders of magnitude weaker than $FGF1^{WT}$ in its ability to induce tyrosine phosphorylation of FGFRs and activation of downstream MAPK signalling (**Fig. 3b**). This loss of signalling ability was mirrored in the diminished mitogenic potential of the chimera in cultured cells compared to $FGF1^{WT}$ ($p<0.001$, unpaired *t*-test) (**Fig. 3c**). We complemented these cell-based data by assessing the mitogenic activity of $FGF1^{\Delta HBS}$-$FGF21^{C\text{-}tail}$ in *C57BL/6* J mice. To do this, animals were injected intravenously with either 2.0 mg/kg body weight

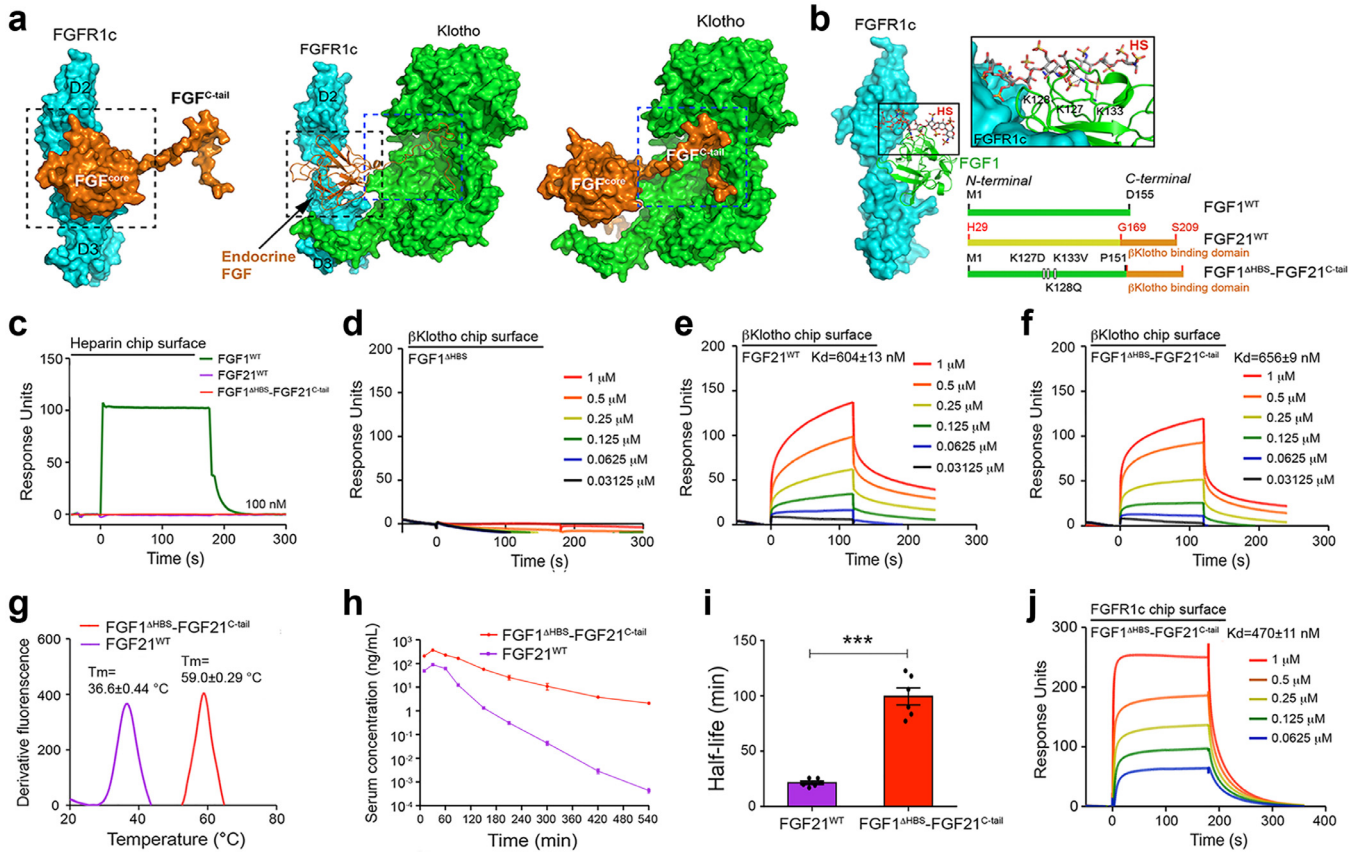

Fig. 2. . **Design and characterization of a thermally stable, high FGFR binding affinity FGF1$^{\Delta HBS}$-FGF21$^{C\text{-}tail}$ chimera**
(a) Core and C-terminal tail regions of endocrine FGFs play independent roles in ternary complex formation. Image at center shows the crystal structure of the FGF23-FGFR1c-αKlotho complex (PDB:5W21); the core and C-tail of endocrine FGF are delineated within dashed black and blue boxes, respectively. In image at left, αKlotho has been removed to visualize the fact that the binding of endocrine FGFs to FGFR is mediated exclusively by the core region. In image at right, the receptor has been removed to illustrate the fact that the unique C-tail of endocrine FGF is specialized for αKlotho co-receptor binding. Endocrine FGF ligand, FGFR1c and Klotho are coloured in orange, cyan and green, respectively. **(b)** Left: crystal structure of the FGF1-FGFR1c complex (PDB ID: 1EVT) with a modeled bound HS oligosaccharide; an expanded view is shown at top right. Modeling of HS is based on the crystal structure of the FGF2-FGFR1c-HS ternary complex (PDB ID: 1FQ9). FGF1^{WT} and FGFR1c are coloured green and cyan, respectively; the HS oligosaccharide carbon backbone is shown in grey sticks. Side chains of three lysine residues of FGF1 predicted to make major contacts with HS are shown as sticks; black dashed lines denote hydrogen bonds. Lower right: Linear representations of human FGF1 (Met1-Asp155) (shown in green), FGF21 (His29-Ser209) (core and C-tail shown in yellow and orange, respectively) and the chimeric molecule FGF1$^{\Delta HBS}$-FGF21$^{C\text{-}tail}$ composed of the HS-binding defective endocrinized FGF1 and the C-terminal tail of FGF21 (Gly169-Ser209). **(c-f)** Representative SPR sensorgrams of HS binding abilities of FGF1^{WT}, FGF21^{WT} and FGF1$^{\Delta HBS}$-FGF21$^{C\text{-}tail}$ (c), βKlotho binding ability of FGF1$^{\Delta HBS}$ (d), FGF21^{WT} (e) and FGF1$^{\Delta HBS}$-FGF21$^{C\text{-}tail}$ (f). **(g)** T_m values of FGF21^{WT} and FGF1$^{\Delta HBS}$-FGF21$^{C\text{-}tail}$ obtained by fluorescence dye-based thermal shift assays. **(h)** Pharmacokinetics of FGF21^{WT} and FGF1$^{\Delta HBS}$-FGF21$^{C\text{-}tail}$ following injection into rats (Log C-T). **(i)** Half-lives of FGF21^{WT} and FGF1$^{\Delta HBS}$-FGF21$^{C\text{-}tail}$ *in vivo* based on the data shown in (h). Data are shown as mean +/- SEM ($n=6$). $^{***}p<0.001$ vs FGF21^{WT} unpaired *t*-test. **(j)** Representative SPR sensorgrams of FGFR1c binding ability of FGF1$^{\Delta HBS}$-FGF21$^{C\text{-}tail}$. In panels c-g, j, the various proteins at the indicated concentrations were passed over the sensor chip containing the indicated immobilized molecule shown in the panels.(For interpretation of the references to colour in this figure legend, the reader is referred to the web version of this article.)

FGF1$^{\Delta HBS}$-FGF21$^{C\text{-}tail}$ or FGF1^{WT} (as a control) for twenty consecutive days. Analysis of the livers from chimera-injected animals showed no evidence of hyperplasia compared to the PBS-treated control (**Fig. 3d–g**). In contrast, injection of FGF1^{WT} caused a clear increase in the number of hyperproliferating liver cells ($p<0.001$, unpaired *t*-test) (**Fig. 3d–g**). Taken together, these *in vitro*, cell-based and *in vivo* data show that the FGF1$^{\Delta HBS}$-FGF21$^{C\text{-}tail}$ chimera has a severely diminished ability to signal in an HS-dependent paracrine fashion.

3.4. FGF1$^{\Delta HBS}$-FGF21$^{C\text{-}tail}$ can signal in a βKlotho dependent manner

We conducted a series of cell-based and *in vivo* experiments to test the βKlotho dependency of the endocrinized FGF1$^{\Delta HBS}$-FGF21$^{C\text{-}tail}$ chimera. To do this, we first explored the chimera's ability to activate its cognate FGFR1c in the context of engineered BaF3 cell lines expressing either FGFR1c alone or co-expressing FGFR1c and βKlotho, as well as in the context of 3T3L1 fibroblast cells. The latter cell line endogenously expresses several FGFRs including FGFR1c, but it lacks βKlotho expression unless it is chemically induced to differentiate into adipocytes [6]. Thus, 3T3L1 cells provide a convenient tool to study the βKlotho-dependency of FGF signalling. Engineered BaF3 cell lines and undifferentiated or differentiated 3T3L1 cells were stimulated with different doses of either the FGF1$^{\Delta HBS}$-FGF21$^{C\text{-}tail}$ chimera or FGF21^{WT} (as a control); total cell lysates were then analyzed using phosphospecific antibodies for FGFR1c and ERK1/2. As previously documented [22], FGF21^{WT} signalling was strictly βKlotho-dependent in both BaF3 and 3T3L1 cell lines (**Fig. 4a–d**). In contrast, high concentrations of FGF1$^{\Delta HBS}$-FGF21$^{C\text{-}tail}$ led to some weak βKlotho-independent signalling (**Fig. 4a and c**), a result that is consistent with the enhanced affinity of FGF1$^{\Delta HBS}$-FGF21$^{C\text{-}tail}$ for FGFR1c. Nevertheless, βKlotho expression dramatically augmented the ability of the chimera to activate FGFR1c in both BaF3 and 3T3L1 cell lines (**Fig. 4b and d**). We further validated these results by quantitative analysis of ERK1/2 phosphorylation. In these experiments, both FGF1$^{\Delta HBS}$-FGF21$^{C\text{-}tail}$ and FGF21^{WT} showed an enhanced ability to activate ERK1/2 signalling in mature adipocytes compared to pre-

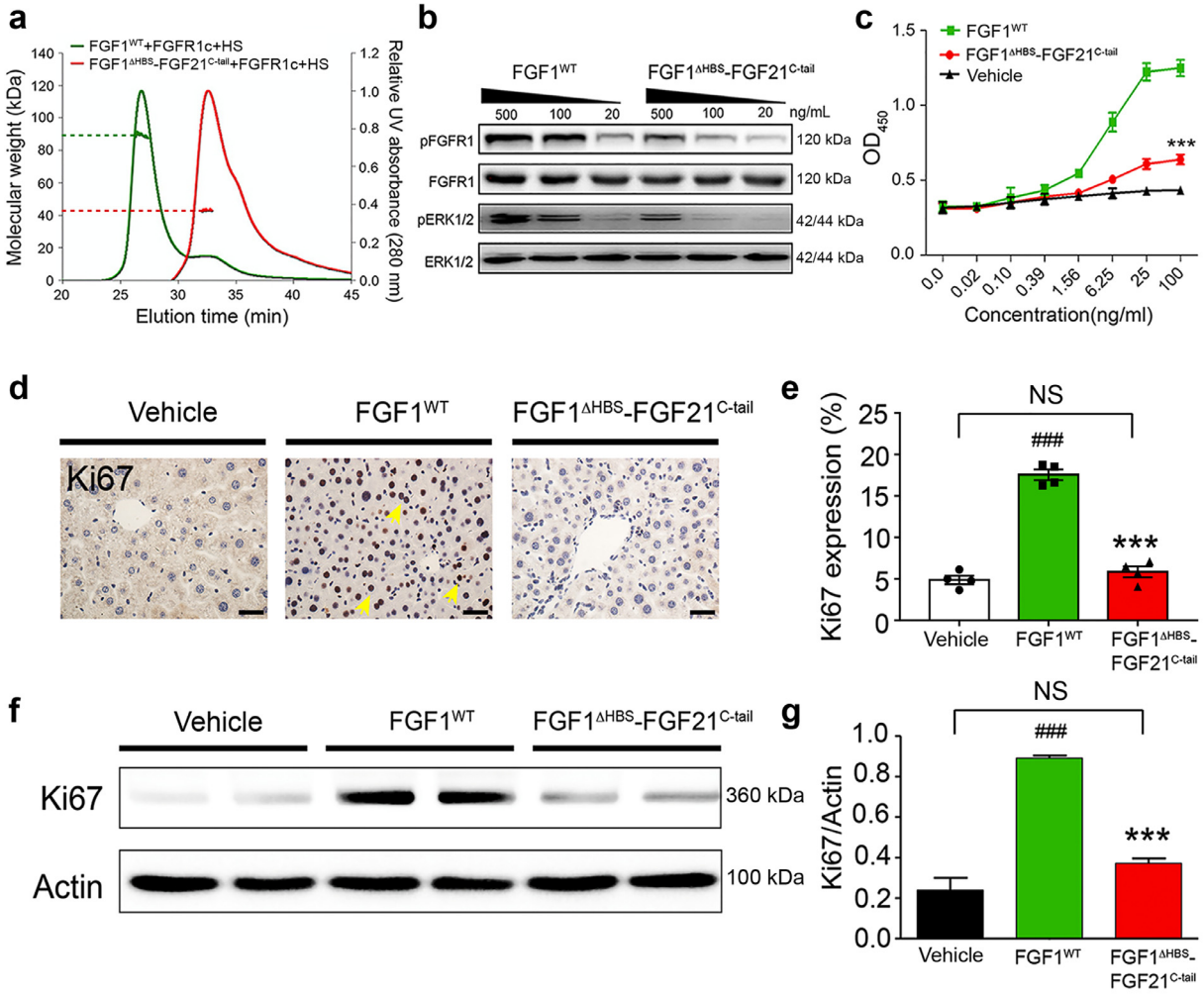

Fig. 3. . FGF1$^{\Delta HBS}$-FGF21$^{C\text{-}tail}$ is impaired in HS-dependent signalling

(a) SEC-MALS analysis of a 1:1:1 stoichiometric mixtures of FGF1, FGFR1c and HS (green) and FGF1$^{\Delta HBS}$-FGF21$^{C\text{-}tail}$, FGFR1c and HS (red). Y axes show scales representing molecular mass (left) and A_{280} (right). Molecular masses of the protein components used were FGF1^{WT} (17.4 kDa), FGF1$^{\Delta HBS}$-FGF21$^{C\text{-}tail}$ (21.0 kDa), FGFR1c ligand-binding domain (25.4 kDa) and HS (3.0 kDa). For each complex, the peak region used for molecular mass determination is demarcated, together with a horizontal dashed line showing the corresponding molecular mass. **(b)** Western blots showing dose-dependent phosphorylation of FGFR1 and ERK1/2 in NIH-3T3 fibroblasts induced by FGF1^{WT} and FGF1$^{\Delta HBS}$-FGF21$^{C\text{-}tail}$ at the concentrations shown. **(c)** NIH-3T3 fibroblast cell proliferation in response to FGF1^{WT} (green), FGF1$^{\Delta HBS}$-FGF21$^{C\text{-}tail}$ (red), or a PBS control (black) using an MTT assay (see Methods). Data from three independent measurements are presented as mean +/- SEM. $^{***}P<0.001$ vs FGF1^{WT}, unpaired *t*-test. **(d)** Liver tissue from C57BL/6 J mice chronically treated by intravenous injection with FGF1^{WT}, FGF1$^{\Delta HBS}$-FGF21$^{C\text{-}tail}$ (2.0 mg/kg body weight per day) or a PBS control (vehicle) were immunostained with an anti-Ki67 antibody. Scale bar, 100 μm. **(e)** Quantitation of immunohistochemical staining data shown in (D) using ImageJ software. Data are presented as mean +/- SEM ($n=4$). $^{###}p<0.001$ vs vehicle; $^{***}p<0.001$ vs FGF1^{WT}, unpaired *t*-test. **(f)** Western blot analysis of Ki67 level in livers from mice chronically treated with FGF1^{WT}, FGF1$^{\Delta HBS}$-FGF21$^{C\text{-}tail}$, or a PBS control (vehicle). An actin loading control is shown below. (**g**) Quantification of western blot results shown in (f) using Image J software. Data are presented as mean +/- SEM ($n=4$). $^{###}p<0.001$ vs vehicle; $^{***}p<0.001$ vs FGF1^{WT}, unpaired *t*-test.(For interpretation of the references to colour in this figure legend, the reader is referred to the web version of this article.)

adipocytes. Notably, the chimera was more potent than FGF21^{WT} in βKlotho-dependent signalling as evidenced by a leftward shift in its dose response curve compared to that of FGF21^{WT} (**Fig. 4e**), presumably reflecting its enhanced FGFR binding ability.

To further corroborate the βKlotho dependency of the chimera, we constructed a βKlotho binding deficient version by introducing a double mutation (Asp192Ala and Tyr207Ala) into the C-terminal tail of FGF1$^{\Delta HBS}$-FGF21$^{C\text{-}tail}$. SPR analysis confirmed that this double mutant (FGF1$^{\Delta HBS}$-FGF21$^{C\text{-}tail\Delta KLB}$) completely failed to bind βKlotho (**Supplementary Fig. 2a**). Importantly, unlike its parent molecule, the FGF1$^{\Delta HBS}$-FGF21$^{C\text{-}tail\Delta KLB}$ mutant showed no evidence of elevated activity in βKlotho-expressing differentiated adipocytes relative to undifferentiated controls (**Supplementary Fig. 2b**). The superior signalling capacity of the FGF1$^{\Delta HBS}$-FGF21$^{C\text{-}tail}$ chimera relative to FGF1$^{\Delta HBS}$ in the presence of βKlotho implies that βKlotho engages the C-tail of FGF1$^{\Delta HBS}$-FGF21$^{C\text{-}tail}$ and the FGFR1c D3 domain so as to impart greater FGF1$^{\Delta HBS}$-FGF21$^{C\text{-}tail}$:FGFR1c complex stability relative to FGF1$^{\Delta HBS}$-FGFR1c.

To complement these cell-based data, we compared the organ distribution of the FGF1$^{\Delta HBS}$-FGF21$^{C\text{-}tail}$ chimera *in vivo* using real-time imaging and functional assays. For real-time imaging, overnight-fasted C57BL/6 J mice were infused intraperitoneally with fluorescent-tagged FGF1$^{\Delta HBS}$-FGF21$^{C\text{-}tail}$ or controls (i.e., FGF1$^{\Delta HBS}$, FGF21^{WT} or FGF1$^{\Delta HBS}$-FGF21$^{C\text{-}tail\Delta KLB}$) and imaged 30 mins post injection. As in the case of FGF21^{WT}, the chimera accumulated in βKlotho-expressing tissues such as epididymal fat (WAT), liver and pancreas (**Fig. 4f**), implying that the presence of the FGF21$^{C\text{-}tail}$ in the chimera is responsible for homing the chimera to these tissues. In contrast, FGF1$^{\Delta HBS}$ and FGF1$^{\Delta HBS}$-FGF21$^{C\text{-}tail\Delta KLB}$ lacked target tissue preference, as they were evenly distributed throughout the body (**Fig. 4f and Supplementary Fig. 2c,d**). To determine functional bio-distribution, a single dose of

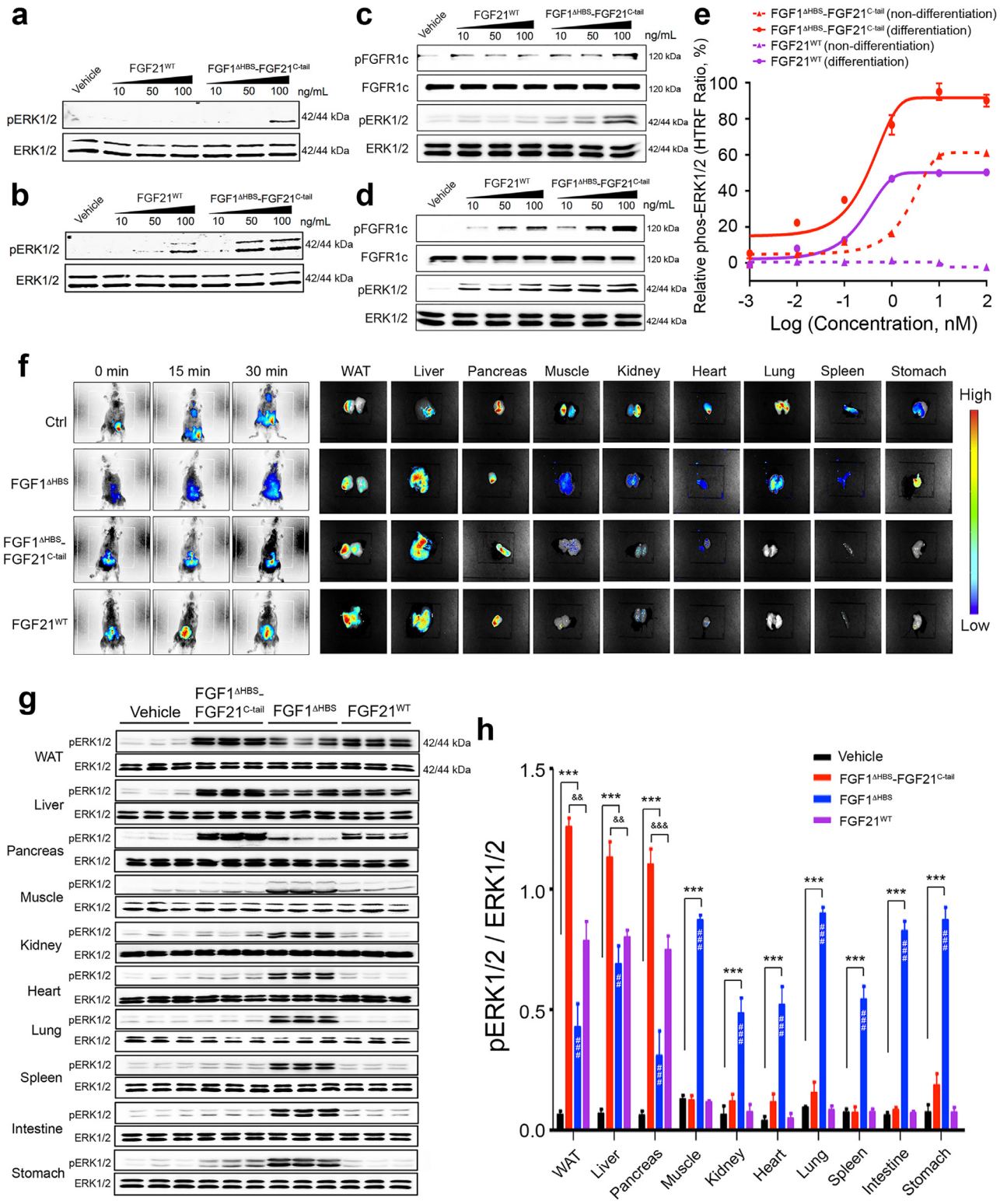

Fig. 4. . ***β*Klotho promotes signalling by the FGF1$^{\Delta HBS}$-FGF21$^{C\text{-}tail}$ chimera**

(a-d) Western blot analyses showing dose-dependent phosphorylation of ERK1/2 induced by FGF21^{WT} and FGF1$^{\Delta HBS}$-FGF21$^{C\text{-}tail}$ in BaF3 cells expressing FGFR1c alone (a), BaF3 cells co-expressing FGFR1c and *β*Klotho (b), and dose-dependent phosphorylation of FGFR1c and ERK1/2 induced by FGF21^{WT} and FGF1$^{\Delta HBS}$-FGF21$^{C\text{-}tail}$ in undifferentiated (c) and differentiated (d) 3T3L1 adipocytes. **(e)** Relative values of ERK1/2 phosphorylation in undifferentiated and differentiated 3T3L1 adipocytes induced by a range of concentrations of FGF21^{WT} and FGF1$^{\Delta HBS}$-FGF21$^{C\text{-}tail}$. $n = 3$/concentration group. **(f)** Left hand panels: Distribution of Alexa 647 Fluor-labeled FGF1$^{\Delta HBS}$-FGF21$^{C\text{-}tail}$, FGF21^{WT} and FGF1$^{\Delta HBS}$ proteins in C57BL/6 J mice at 0, 15 and 30 mins post-intraperitoneal injection (0.5 mg/kg body weight). Right hand panels: Ex vivo fluorescence imaging of the indicated organs harvested from the same mice. Injection with fluorescent dye alone was used as a control (Ctrl). Vertical scale at right shows colour correspondence with fluorescent intensity. **(g)** Western blot analyses of ERK1/2 phosphorylation in lysates prepared from WAT, liver, pancreas, muscle, kidney, heart, lung, spleen, small intestine and stomach from C57BL/6 J mice 30 min after subcutaneous injection with PBS (vehicle), FGF1$^{\Delta HBS}$-FGF21$^{C\text{-}tail}$, FGF1$^{\Delta HBS}$ or FGF21^{WT} (0.5 mg/kg body weight). For each tissue, an ERK1/2 antibody was used as a loading control. (**h**) Quantitation of western blot data from (g) using Image J software. Data are presented as mean +/- SEM ($n = 6$). $^{***}p<0.001$, FGF1$^{\Delta HBS}$, FGF21^{WT} and/or FGF1$^{\Delta HBS}$-FGF21$^{C\text{-}tail}$ vs vehicle; $^{\#\#}p<0.01$, $^{\#\#\#}p<0.001$, FGF1$^{\Delta HBS}$ vs FGF1$^{\Delta HBS}$-FGF21$^{C\text{-}tail}$; $^{\&\&}p<0.01$, $^{\&\&\&}p<0.001$, FGF21^{WT} vs FGF1$^{\Delta HBS}$-FGF21$^{C\text{-}tail}$, unpaired *t*-test.

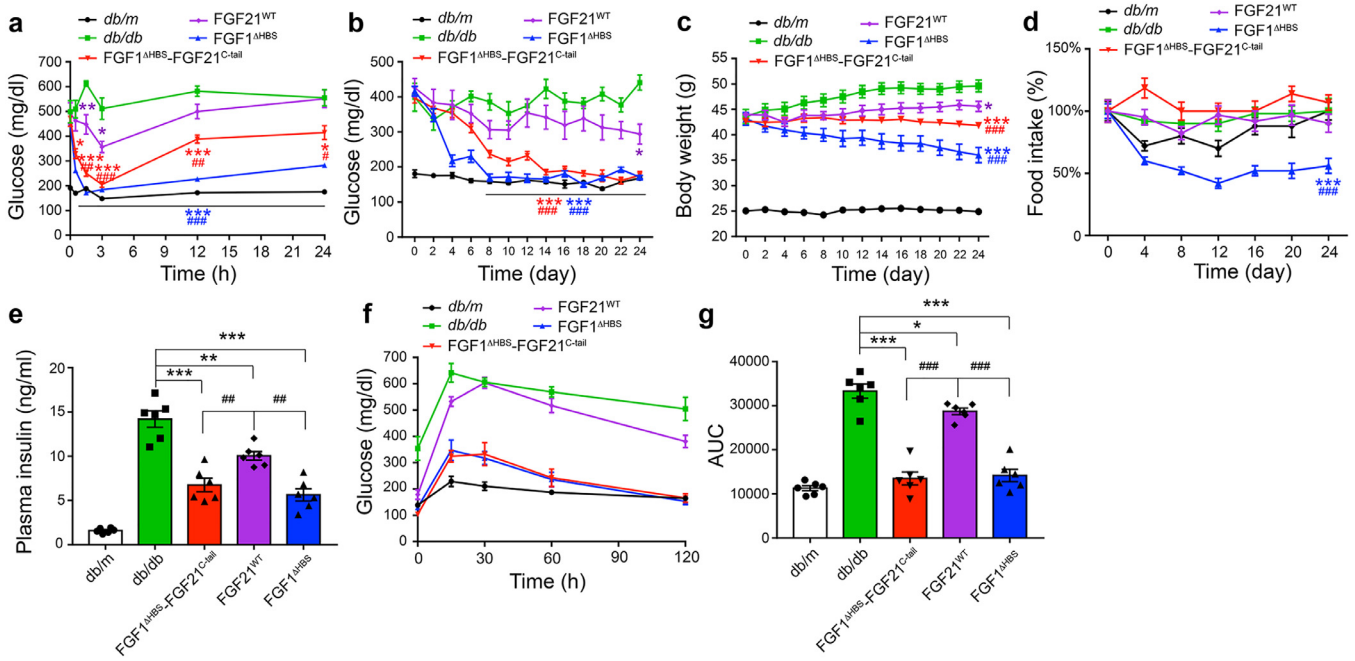

Fig. 5. . Effects of FGF1$^{\Delta HBS}$-FGF21$^{C\text{-}tail}$ on blood glucose levels and insulin sensitivity in *db/db* mice
(a) Changes in blood glucose levels of *db/db* mice following an acute intraperitoneal injection of FGF1$^{\Delta HBS}$-FGF21$^{C\text{-}tail}$, FGF21^{WT} or FGF1$^{\Delta HBS}$ (0.5 mg/kg body weight) over the course of 24 h; *db/db* mice treated with buffer alone (PBS) and their littermates (*db/m*) served as controls. Data are presented as mean +/- SEM ($n = 5$). $^{*}p<0.05$, $^{**}p<0.01$, $^{***}p<0.001$ vs *db/db*; $^{\#}p<0.05$, $^{\#\#}p<0.01$, $^{\#\#\#}p<0.001$ vs FGF21^{WT} treatment, unpaired *t*-test. **(b–d)** Fed-state blood glucose levels (b), body weight (c) and food intake (d) of *db/db* mice over the course of 24 days of daily subcutaneous administration of FGF1$^{\Delta HBS}$-FGF21$^{C\text{-}tail}$, FGF21^{WT} or FGF1$^{\Delta HBS}$ (0.5 mg/kg body weight). Data are presented as mean +/- SEM ($n = 6$). $^{*}p<0.05$, $^{***}p<0.001$ vs *db/db*; $^{\#\#\#}p<0.001$ vs FGF21^{WT} treatment, unpaired *t*-test. **(e)** Serum insulin levels of *db/db* mice after a 24-day course of treatment with FGF1$^{\Delta HBS}$-FGF21$^{C\text{-}tail}$, FGF21^{WT} or FGF1$^{\Delta HBS}$ administered as in (b). Data are presented as mean +/- SEM ($n = 6$). $^{**}p<0.01$, $^{***}p<0.001$ vs *db/db*; $^{\#\#}p<0.01$ vs FGF21^{WT} treatment, unpaired *t*-test. **(f,g)** Glucose tolerance test in *db/db* mice performed 12 h after the final injection (on day 24) of sequential administration with FGF1$^{\Delta HBS}$-FGF21$^{C\text{-}tail}$, FGF21^{WT} or FGF1$^{\Delta HBS}$ as detailed in (b). Changes in blood glucose levels (e) and integrated area under the curve (AUC) (f) are shown. Data are presented as mean +/- SEM ($n = 6$). $^{*}p<0.05$, $^{***}p<0.001$ vs *db/db*; $^{\#\#\#}p<0.001$ vs FGF21^{WT} treatment, unpaired *t*-test.

FGF1$^{\Delta HBS}$-FGF21$^{C\text{-}tail}$, FGF1$^{\Delta HBS}$ or FGF21^{WT} (the latter two as controls) were injected into C57BL/J6 mice. After 30 min, epididymal fat, liver, pancreas, muscle, kidney, heart, lung, spleen, small intestine, and stomach were harvested and analyzed for the presence of ERK1/2 phosphorylation by Western blotting as a readout for FGF signalling. As in the case of FGF21^{WT}, the chimera preferentially signalled in fat, liver and pancreas (**Fig. 4g,h**), implying that the presence of the FGF21 C-tail in the chimera is selectively recognized by these βKlotho expressing tissues. Importantly, consistent with our cell-based data (**Fig. 4b and d**), the chimera was more potent than FGF21^{WT} in activating ERK1/2 *in vivo* ($p<0.001$; $p<0.01$, unpaired *t*-test) (**Fig. 4g,h**). In contrast, FGF1$^{\Delta HBS}$ had no such tissue target selectivity, indiscriminately activating the ERK1/2 pathway in all tissues tested (**Fig. 4g,h**).

3.5. FGF1$^{\Delta HBS}$-FGF21$^{C\text{-}tail}$ is pharmacologically superior to FGF21^{WT} in regulating blood glucose and insulin sensitivity

We assessed the potency of the FGF1$^{\Delta HBS}$-FGF21$^{C\text{-}tail}$ chimera in alleviating hyperglycemia in a *db/db* diabetic mouse model; FGF21^{WT} and FGF1$^{\Delta HBS}$ were used as controls. An acute injection of either the chimera or FGF1$^{\Delta HBS}$ (each at 0.5 mg/kg body weight) lowered blood glucose to a normal level within 3 h, with an effect lasting up to 24 h. In contrast, FGF21^{WT} produced a much weaker glucose lowering effect ($p<0.001$; $p<0.01$; $p<0.05$, unpaired *t*-test) (**Fig. 5a**). This difference was more pronounced at a lower ligand concentration: at a dose of 0.125 mg/kg body weight, FGF21^{WT} essentially lacked glucose-lowering activity, whereas FGF1$^{\Delta HBS}$-FGF21$^{C\text{-}tail}$ still exerted robust activity, especially within the first 3 h post-administration ($p<0.001$; $p<0.01$; $p<0.05$, unpaired *t*-test) (**Supplementary Fig. 3a**).

We also compared the effects of chronic administration of the chimera, FGF21^{WT} and FGF1$^{\Delta HBS}$ in *db/db* mice over a period of 24 days. Consistent with our acute dose injection data, daily administration of FGF21^{WT} led to a modest but significant reduction in glucose levels ($p<0.05$, unpaired *t*-test) (**Fig. 5b**) resembling that seen following administration of insulin, the classic treatment for hyperglycemia in type 2 diabetes ($p<0.001$; $p<0.05$, unpaired *t*-test) (**Supplementary Fig. 3b**). In contrast, both the chimera and FGF1$^{\Delta HBS}$ robustly lowered blood glucose to a normal level without causing hypoglycemia ($p<0.001$, unpaired *t*-test) (**Fig. 5b**). In obese mice, chronic administration of FGF21 has been shown to cause beneficial weight loss [44]. We therefore studied the effect on body mass following chronic administration of FGF1$^{\Delta HBS}$-FGF21$^{C\text{-}tail}$. We found that the chimera had a greater potency compared to FGF21^{WT} in reducing the body mass of *db/db* mice ($p<0.001$, unpaired *t*-test) (**Fig. 5c**), without causing any significant adverse effect on appetite or food intake (**Fig. 5d**). In contrast, as previously reported for FGF1^{WT} [45], *db/db* mice treated daily with FGF1$^{\Delta HBS}$ had a markedly reduced food intake and a corresponding loss of body mass ($p<0.001$, unpaired *t*-test) (**Fig. 5c,d**). Moreover, long-term administration of the chimera did not cause detectable liver proliferation, nor did this treatment induce expression of hepatocarcinoma related genes in the livers of *db/db* mice (**Supplementary Fig. 4a–c**). Notably, long-term administration of the chimera was also accompanied by desirable changes in the levels of several metabolic parameters, including insulin ($p<0.001$; $p<0.01$, unpaired *t*-test) (**Fig. 5e**), glycated serum protein (GSP) and C-Peptide ($p<0.01$, unpaired *t*-test) (**Supplementary Fig. 5a,b**). The chimera showed greater efficacy compared with FGF21^{WT} in improving insulin sensitivity as measured by a glucose tolerance test (GTT) ($p<0.001$, unpaired *t*-test) (**Fig. 5f,g**). We conclude that the

superior pharmacodynamics/kinetics of FGF1$^{\Delta HBS}$-FGF21$^{C\text{-}tail}$ is a consequence of its greater stability and receptor binding affinity compared to FGF21^{WT}.

We also explored the potential of parenteral administration of FGF1$^{\Delta HBS}$-FGF21$^{C\text{-}tail}$ in diabetic therapy. We found that *db/db* mice chronically treated with FGF1$^{\Delta HBS}$-FGF21$^{C\text{-}tail}$ were phenotypically normal in terms of locomotor activity, O_2 consumption, CO_2 production and respiratory exchange ratio ($p<0.001$; $p<0.01$; $p<0.05$, unpaired *t*-test) **(Supplementary Fig. 6)**. These data suggest that chronic treatment with FGF1$^{\Delta HBS}$-FGF21$^{C\text{-}tail}$ does not elicit adverse pleiotropic effects, at least in mouse models.

To establish a basis for clinical trials, we monitored the appetite of healthy cynomolgus monkeys following chronic daily administration of the chimera; FGF21^{WT}, FGF1$^{\Delta HBS}$ and buffer alone were used as controls (**Supplementary Fig. 7**). As in the case of FGF21^{WT}, the chimera had no adverse impact on food intake or body weight, whereas administration of FGF1$^{\Delta HBS}$ led to a dramatic loss of appetite and ultimately to a substantial reduction of body mass (**Supplementary Fig. 7b,c and Tables S3–5**). Notably, all cynomolgus monkeys survived to their scheduled autopsies, with the single exception of an FGF1$^{\Delta HBS}$-treated female which died on day 18 **(Supplementary Fig. 7b)**.

3.6. FGF1$^{\Delta HBS}$-FGF21$^{C\text{-}tail}$ is more potent than FGF21 in adipose remodeling

Obesity is characterized by increased fat stores and an expansion of WAT, largely as a result of an increase in the size of adipocytes [46,47]. We found that treatment of *db/db* mice with either FGF1$^{\Delta HBS}$-FGF21$^{C\text{-}tail}$ or FGF21^{WT} reduced the size of both white and brown adipocytes ($p<0.001$; $p<0.01$, unpaired *t*-test) (**Fig. 6a–c**), and was accompanied by progressive body weight loss during the course of 24 days' treatment. Notably, the chimera was conspicuously more potent in reducing fat mass and adipocyte size than FGF21^{WT} ($p<0.01$; $p<0.05$, unpaired *t*-test) (**Fig. 6a,b**). Moreover, *db/db* mice treated with FGF1$^{\Delta HBS}$-FGF21$^{C\text{-}tail}$ exhibited consistently enhanced phosphorylation of AKT in adipose tissue compared to mice treated with FGF21^{WT} ($p<0.01$, unpaired *t*-test) (**Fig. 6d,e**), implying a more potent insulin-sensitizing activity of FGF1$^{\Delta HBS}$-FGF21$^{C\text{-}tail}$ compared to FGF21^{WT}. FGF21 has been shown to lower blood glucose via upregulation of glucose transporter 1 (GLUT1) [6,48–50]. Consistent with these data, we found that FGF1$^{\Delta HBS}$-FGF21$^{C\text{-}tail}$ was more potent than FGF21^{WT} in resolving impaired GLUT1 translocation in the WAT of *db/db* mice ($p<0.01$, unpaired *t*-test) (**Fig. 6f,g**). The stimulatory effect of FGF21^{WT} on the conversion of white to brown adipose tissues ("browning") has also been well documented [51]. We therefore compared the effects of FGF$^{\Delta HBS}$-FGF21$^{C\text{-}tail}$ and FGF21^{WT} on the expression of peroxisome proliferator-activated receptor-gamma coactivator (PGC-1α) and uncoupling protein-1 (UCP-1), two representative markers of adipose browning and thermogenesis. We found that treatment with FGF$^{\Delta HBS}$-FGF21$^{C\text{-}tail}$ resulted in a greater enhancement in the expression of these two genes in subcutaneous white adipose tissue compared to FGF21^{WT} ($p<0.001$; $p<0.01$, unpaired *t*-test) (**Fig. 6h,i**).

3.7. Long-term effects of FGF1$^{\Delta HBS}$-FGF21$^{C\text{-}tail}$ on hepatic steatosis

We further compared the effects of FGF1$^{\Delta HBS}$-FGF21$^{C\text{-}tail}$ and FGF21^{WT} on hepatic steatosis in *db/db* mice. We found that daily administration with FGF1$^{\Delta HBS}$-FGF21$^{C\text{-}tail}$ over 24 days reduced the liver mass to a significantly greater extent compared to FGF21^{WT} ($p<0.05$, unpaired *t*-test) (**Fig. 7a**). Concomitantly, histological staining and biochemical analyses showed that chronic treatment of *db/db* mice with FGF1$^{\Delta HBS}$-FGF21$^{C\text{-}tail}$ caused a greater attenuation of hepatic steatosis (**Fig. 7b**) and a greater reduction in liver triglycerides (TGs) compared to FGF21^{WT} ($p<0.05$, unpaired *t*-test) (**Fig. 7c**). Consistent with these histological findings, we found enhanced reductions in the injury markers alanine transaminase (ALT) and aspartate transaminase (AST) in the livers of *db/db* mice treated with the chimera compared to the livers of animals treated with FGF21^{WT} ($p<0.05$, unpaired *t*-test) (**Fig. 7d,e**). These relative changes were mirrored by corresponding reductions in serum levels of ALT, AST and non-essential fatty acids (NEFA) ($p<0.001$; $p<0.01$, unpaired *t*-test) (**Supplementary Fig. 5c–e**). The decreased lipid accumulation in hepatic tissues implies a decline in lipogenesis (lipid synthesis) and lipid storage in the FGF1$^{\Delta HBS}$-FGF21$^{C\text{-}tail}$ treatment group. This was confirmed by our contemporaneous finding of lowered expression of fatty acid synthase (FAS) and stearoyl-CoA desaturase (SCD-1) in hepatic tissues ($p<0.01$; $p<0.05$, unpaired *t*-test) (**Fig. 7f,g**). We also analyzed acetyl CoA carboxylase (ACC) phosphorylation and carnitine palmitoyl transferase-1α (CPT-1α) expression as readouts for activation of β-oxidation pathways in the livers of *db/db* mice treated with either FGF21^{WT} or the chimera, and found that FGF1$^{\Delta HBS}$-FGF21$^{C\text{-}tail}$ has a significantly greater ability to stimulate β-oxidation relative to FGF21^{WT} ($p<0.05$, unpaired *t*-test) (**Fig. 7f,h**).

3.8. FGF1$^{\Delta HBS}$-FGF21$^{C\text{-}tail}$ functions as an insulin sensitizer in non-human primates with T2D

Lastly, we studied the ability of the chimera to exert glycemic control in spontaneous diabetic cynomolgus monkeys (**Fig. 8 and Tables S6-S8**) as a model for human T2D [52–55]. We found that 15 days of daily administration of FGF1$^{\Delta HBS}$-FGF21$^{C\text{-}tail}$ at a low dose (0.05 mg/kg) was sufficient to induce a significant glucose-lowering effect ($p<0.01$; $p<0.05$, unpaired *t*-test) (**Fig. 8a,b**). This effect was stable following a secondary 15-day period of daily administration at a higher dose (0.15 mg/kg) without evidence of hypoglycemia (**Fig. 8a,b**). We also found a significant but short-lived reduction in food intake during the first few days following low-dose administration of the chimera. This transient effect was more pronounced and persistent following high-dose treatment (**Table S7**). These changes in appetite in FGF1$^{\Delta HBS}$-FGF21$^{C\text{-}tail}$ treated animals were accompanied by slight changes in body weight relative to pre-treatment (**Table S7**). We also noted some weight loss in the saline control group, possibly ascribable to environmental stress; similar phenomena have been reported in previous studies [56].

To further evaluate the effect of FGF1$^{\Delta HBS}$-FGF21$^{C\text{-}tail}$ on glucose homeostasis, we subjected T2D monkeys to an oral glucose tolerance test (OGTT). We found a reduction in glucose levels over the course of 3 hr at each of the doses administered, with a significantly greater effect at the higher dose (**Fig. 8c**). Concomitantly, there was a substantially greater decrease in serum insulin level in high-dose treated animals compared to those receiving low-dose treatment (**Fig. 8d**). Consistent with these data, serum levels of hemoglogin A1C (HbAIc, a marker for severity of hyperglycemia) was also reduced by the chimera (**Fig. 8e**). We also monitored total cholesterol (TCHO) and low-density lipoprotein (LDL) levels, and found modest but statistically significant reductions as a result of administration of FGF1$^{\Delta HBS}$-FGF21$^{C\text{-}tail}$ at a high dose ($p<0.01$; $p<0.05$, unpaired *t*-test) (**Fig. 8f,g and Table S8**). Taken together, our data suggest that FGF1$^{\Delta HBS}$-FGF21$^{C\text{-}tail}$ administration improves glucose homeostasis in T2D monkeys principally by dampening insulin resistance and suppressing appetite.

4. Discussion

We devised and implemented a structure-based chimerisation approach that effectively mitigates both the intrinsically weak receptor binding affinities and short half-lives of endocrine FGFs.

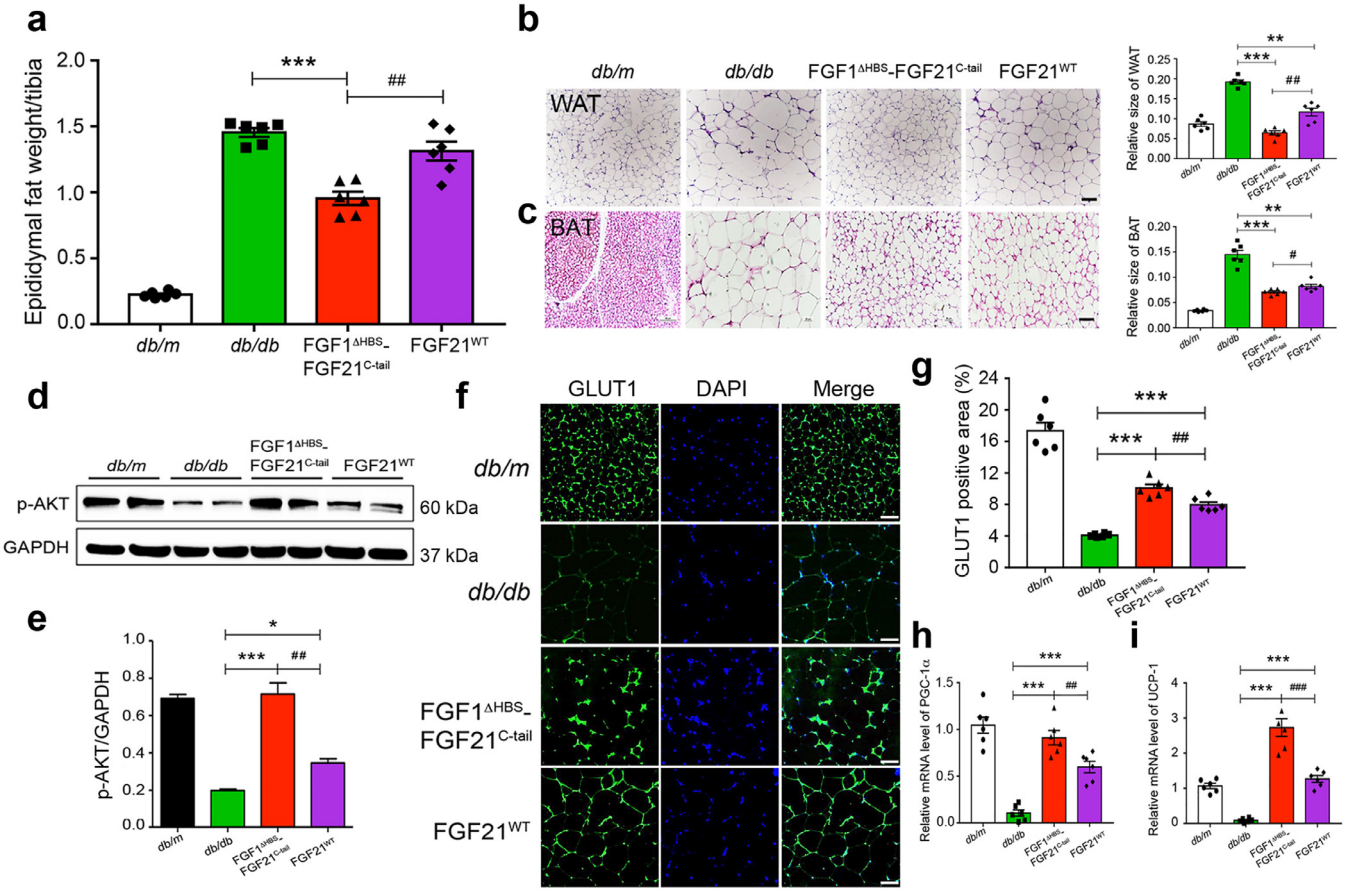

Fig. 6. . Chronic Effects of FGF1$^{\Delta HBS}$-FGF21$^{C\text{-}tail}$ on adipose remodeling in *db/db* mice

Adipose tissues were isolated from *db/db* mice treated with FGF1$^{\Delta HBS}$-FGF21$^{C\text{-}tail}$ or FGF21 for 24 days (0.5 mg/kg body weight); corresponding tissues from *db/db* mice treated with buffer alone (PBS) and their littermates (*db/m*) served as controls. **(a)** Epididymal fat weight of *db/db* mice treated with FGF1$^{\Delta HBS}$-FGF21$^{C\text{-}tail}$ or FGF21^{WT}. Data are presented as mean +/- SEM ($n = 6$). $^{***}p<0.001$ vs *db/db*; $^{\#\#}p<0.01$ vs FGF21^{WT} treatment, unpaired *t*-test. **(b,c)** Images of WAT (b) and brown adipose tissue (BAT) (c) sections stained with hematoxylin and eosin (H&E). Data are representative of 6 mice from each group. Scale bar, 100 μm. Right hand panels: relative adipocyte sizes calculated from H&E stained sections (Relative sizes=unit area/ the cell number per unit area). Data are presented as mean +/- SEM ($n = 6$). $^{**}p<0.01$, $^{***}p<0.01$ vs *db/db*; $^{\#}p<0.05$, $^{\#\#}p<0.01$ vs FGF21^{WT} treatment, unpaired *t*-test. **(d,e)** Western blot analysis for Epi-WAT AKT phosphorylation and its quantitation by image J. Data are presented as mean +/- SEM ($n = 6$). $^{*}p<0.05$, $^{***}p<0.001$ vs *db/db*; $^{\#\#}p<0.01$ vs FGF21^{WT} treatment, unpaired *t*-test. **(f,g)** Enhanced translocation of GLUT1 in Epi-WAT as measured by immunofluorescence staining (f) and quantified by image J (g). Data are representative of 6 mice from each group; $^{***}p<0.001$ vs *db/db*; $^{\#\#\#}p<0.001$ vs FGF21^{WT} treatment, unpaired *t*-test. Scale bar, 100 μm. **(h,i)** Real-time quantitative PCR analysis of mRNAs encoding PGC-1α (h) and UCP-1 (i) in subcutaneous adipose tissue. Data are presented as mean +/- SEM ($n = 6$). $^{***}p<0.001$ vs *db/db*; $^{\#\#}p<0.01$, $^{\#\#\#}p<0.001$ vs FGF21^{WT} treatment, unpaired *t*-test.

Such endocrine FGF analogs are therefore potentially clinically useful. The practicality of the strategy we developed is established by the fact that a rationally engineered chimera, FGF1$^{\Delta HBS}$-FGF21$^{C\text{-}tail}$, is both potent and long-acting while retaining its βKlotho dependency (**Figs. 2 and 4**).

The longer half-life of the chimera is in all likelihood attributable to its increased thermal stability; nonetheless, we cannot exclude the possibility that additional factors such as reduced excretion, tissue clearance, or proteolytic degradation may also contribute. Indeed, relative to native FGF21, the chimera would be expected to be less prone to proteolysis because of its structurally more rigid core. In common with FGF1$^{\Delta HBS37}$, the chimera has a diminished ability to signal in an HS-dependent fashion, and accordingly has a severely suppressed ability to induce unwanted HS-dependent FGFR signaling and cellular proliferation (**Fig. 3**). However, unlike FGF1$^{\Delta HBS}$, the chimera has an enhanced signalling capacity in βklotho-expressing cultured cells, and acts *in vivo* primarily in βklotho-expressing adipose and liver tissues (**Fig. 4**). Thus, FGF1$^{\Delta HBS}$-FGF21$^{C\text{-}tail}$, but not FGF1$^{\Delta HBS}$, is a functional analog of FGF21^{WT}. Notably, while FGF1$^{\Delta HBS}$ causes a severely diminished appetite with accompanying weight loss in *db/db* mice and in monkeys, like FGF21^{WT}, the chimera is neutral with respect to these parameters (**Fig. 5 and Supplementary Fig. 7**). We attribute these differences to the absence of FGF1$^{\Delta HBS}$ tissue target specificity.

Systemic administration of recombinant human FGF21 has been reported to significantly reverse hepatic steatosis and fatty liver in a T2D animal model [7,44,57]. Additionally, in obese humans, administration of an FGF21 analog can significantly improve dyslipidemia by decreasing TG levels and shifting to a potentially less atherogenic apolipoprotein concentration profile [58]. Moreover, FGF21 and its analogs or mimetics have been reported to be capable of improving glucose homeostasis in rodents and in primates [59–61]. Our chimera is superior to FGF21^{WT} in reducing body weight and in ameliorating fatty liver in *db/db* mice (**Figs. 5–7**), and exerts a significant beneficial glucose lowering effect in spontaneous diabetic cynomolgus monkeys (**Fig. 8**). This is in marked contrast to the absence of the hypoglycemic effect elicited by LY2405319 (a pegylated form of FGF21) [58] or PF-05231023 (two modified FGF21 molecules linked to a humanized immunoglobulin 1 (IgG1) monoclonal antibody backbone) [62]. We note that the minimal effects of the chimera on serum lipid parameters in spontaneous diabetic cynomolgus monkeys probably

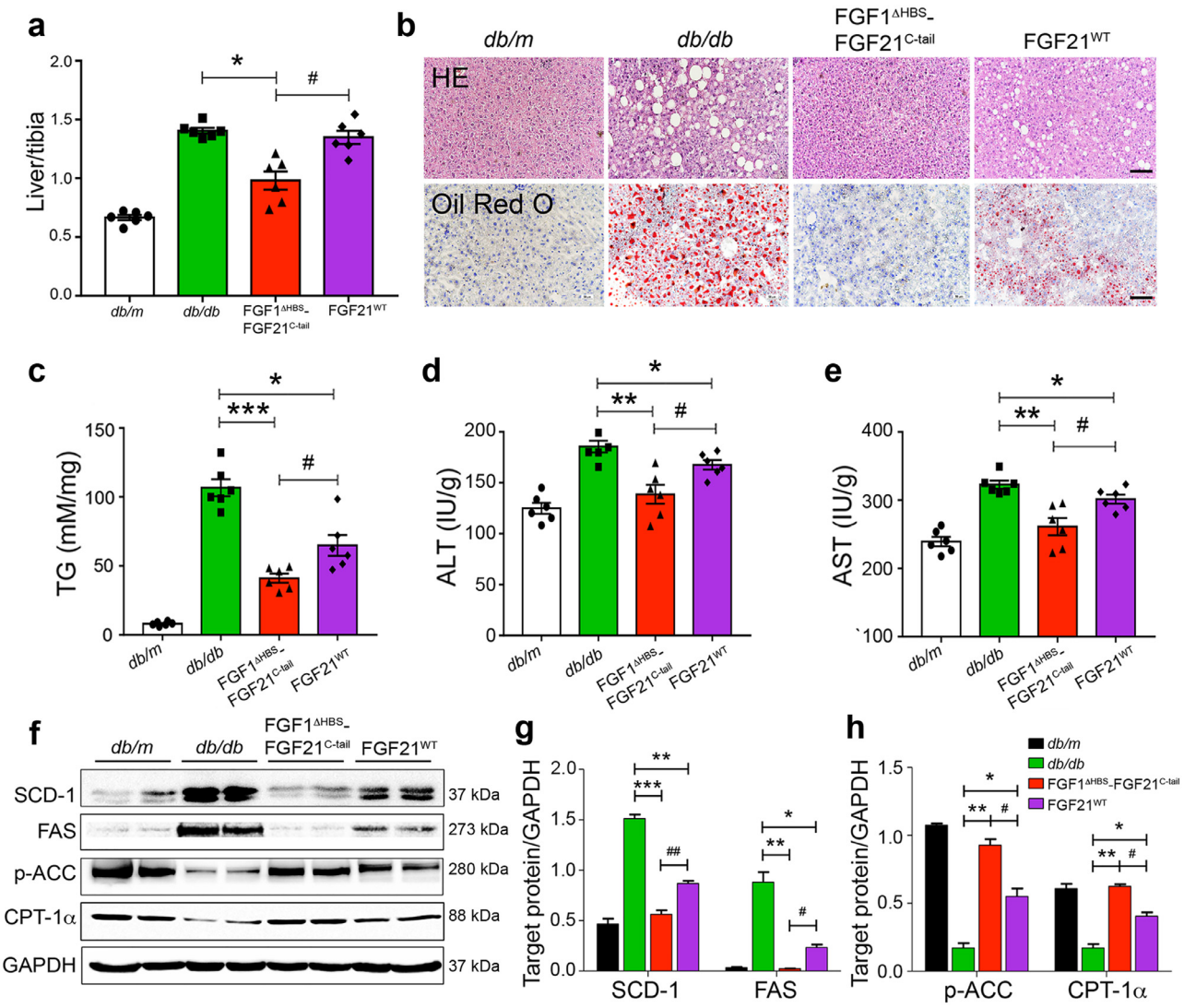

Fig. 7. . **Effects of FGF1$^{\Delta HBS}$-FGF21$^{C\text{-}tail}$ on hepatic steatosis and lipid metabolism in *db/db* mice**
The *db/db* mice were chronically treated by daily subcutaneous injection of PBS alone (as a control) or FGF1$^{\Delta HBS}$-FGF21$^{C\text{-}tail}$ or FGF21^{WT} proteins (0.5 mg/kg body weight per day) over the course of 24 days. **(a)** Changes in liver mass of *db/db* mice. Data are presented as mean +/- SEM ($n = 6$). $^{*}p<0.05$ vs *db/db*, $^{\#}p<0.05$ vs FGF21^{WT} treatment, unpaired *t*-test. **(b)** Images of liver tissue sections stained with hematoxylin and eosin (H&E) (upper panel) or Oil Red O (lower panel). Red dots in the Oil Red O stained tissue sections are indicative of micro- and macro-vesicular steatosis; note the greater improvement following administration of the chimera compared to administration of FGF21^{WT}. Data are representative of 6 mice per group. Scale bar, 100 µm. (**c–e**) Triglyceride (TG) (c), alanine transaminase (ALT) (d) and aspartate transaminase (AST) (e) levels in liver extracts (see Methods). Data are presented as mean +/- SEM ($n = 6$). $^{*}p<0.05$, $^{**}p<0.01$, $^{***}p<0.001$ vs *db/db;* $^{\#}p<0.05$ vs FGF21^{WT} treatment, unpaired *t*-test. **(f)** Western blot analyses of liver tissues of *db/db* mice following 24-day chronic treatment with FGF1$^{\Delta HBS}$-FGF21$^{C\text{-}tail}$. Note the inhibition of expression of SCD-1 and FAS and enhancement of ACC phosphorylation and CPT-1a expression. **(g,h)** Densitometric quantification of Western blot data shown in (f). Data are presented as mean +/- SEM ($n = 6$). $^{*}p<0.05$, $^{**}p<0.01$, $^{***}p<0.001$ vs *db/db;* $^{\#}p<0.05$, $^{\#\#}p<0.01$ vs FGF21^{WT} treatment, unpaired *t*-test.

reflects the fact that at the outset, these animals do not have significantly elevated serum lipids [63–65].

Our chimerisation approach circumvents the shortcomings associated with modification-intensive PEGylation or Fc fusion strategies, including an inherent risk of compromised efficacy [66,67]. Moreover, our chimeric FGF21 is unlikely to trigger an undesired immune response: only the point of fusion offers a remote risk for the generation of a novel epitope. Given these considerations, our approach holds significant promise as a paradigm for a new generation of FGF21-based anti-diabetic therapies. A similar strategy could readily be adapted to FGF19 and FGF23, both of which – in common with FGF21 – lack the stability and potency required for clinical application.

Declaration of Competing Interest

The authors declared that they have no competing interests.

Author contribution

L.Z., J.N., H.L., J.Z., Y.L., Z.S., C.X., X.W., Y.Y., X.L., M.M. Z.H researched the data. X.L., M.M., Z.H contributed to the initial discussion and design of the project. J.N., M.M., Z.H wrote the manuscript. Z.H is the guarantor of this work and, as such, had full access to all the data in the study and takes responsibility for the integrity of the data and the accuracy of the data analysis.

Acknowledgements

This work was supported by Grants from National Key R&D Program of China(2017YFA0506000) (to X.L. and Z.H.),

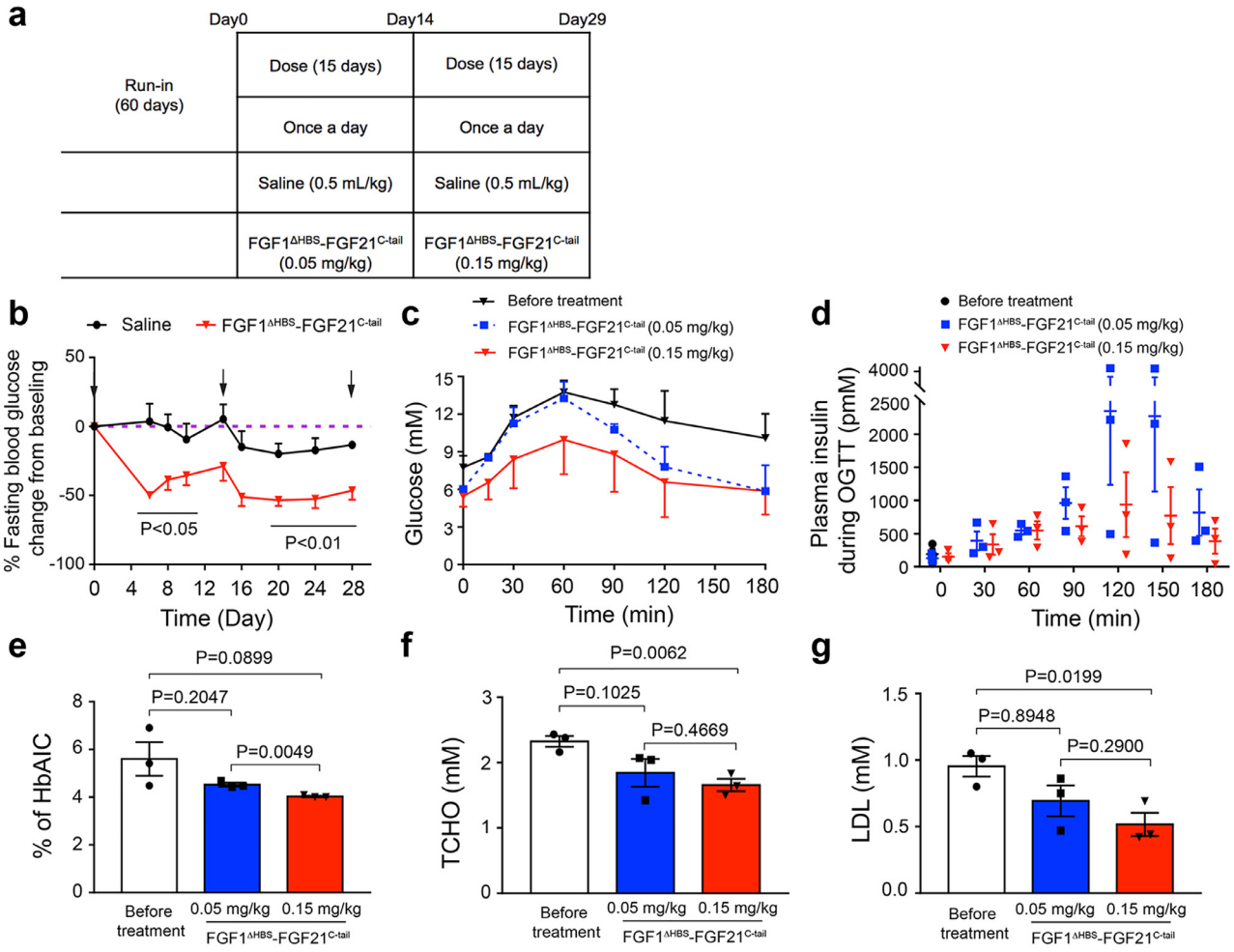

Fig. 8. . Effect of the FGF1$^{\Delta HBS}$-FGF21$^{C\text{-}tail}$ Chimera on Metabolic Regulation in Cynomolgus Monkeys with T2D
(a) Study Design. A total of 6 spontaneous diabetic cynomolgus monkeys (4 male and 2 female) were included in this study. The first dose of FGF1$^{\Delta HBS}$-FGF21$^{C\text{-}tail}$ chimera was administered on day 0. **(b)** Changes from baseline values following administration of FGF1$^{\Delta HBS}$-FGF21$^{C\text{-}tail}$ for fasting blood glucose. Arrows in (b) indicate the times at which glucose tolerance tests were done. **(c,d)** Changes in glucose levels (c) and plasma insulin (d) during OGTTs done following administration of a low or high dose of chimera. **(e)** Percent change in HbAlc between day 0 and following 15 days of treatment with a low or high dose of chimera. **(f,g)** Changes of plasma TCHO (f) and LDL (g) lipoprotein profiles in animals treated with chimera FGF1$^{\Delta HBS}$-FGF21$^{C\text{-}tail}$ between before treatment and after administration of a low or high different doses. Data are presented as mean +/- SEM ($n = 3$). Significance is indicated by P values comparing levels before and following administration of different doses of chimera (unpaired t-test).

Natural Science Foundation of China (81874323 and 81803415 to Z.H and J.N.), Ten-thousand Talents Programs of China and Zhejiang (Z.H), Key Project from Science Technology Department of Zhejiang Province (2017C030330) & Wenzhou (ZS2017013) (to Z.H.), Project from Science Technology Department of Wenzhou(Y20160163) (to L.Z.) and the U.S. National Institutes of Health NIDCRGrant DE13686 (to M.M.).

Supplementary materials

Supplementary material associated with this article can be found, in the online version, at doi:10.1016/j.ebiom.2019.09.052.

References

[1] Goetz R, Mohammadi M. Exploring mechanisms of FGF signalling through the lens of structural biology. Nat Rev Mole Cell Biol 2013;14(3):166–80.
[2] Degirolamo C, Sabba C, Moschetta A. Therapeutic potential of the endocrine fibroblast growth factors FGF19, FGF21 and FGF23. Nat Rev Drug Discov 2016;15(1):51–69.
[3] Inagaki T, Choi M, Moschetta A, et al. Fibroblast growth factor 15 functions as an enterohepatic signal to regulate bile acid homeostasis. Cell Metab 2005;2(4):217–25.
[4] Fu L, John LM, Adams SH, et al. Fibroblast growth factor 19 increases metabolic rate and reverses dietary and leptin-deficient diabetes. Endocrinology 2004;145(6):2594–603.
[5] Xie MH, Holcomb I, Deuel B, et al. FGF-19, a novel fibroblast growth factor with unique specificity for FGFR4. Cytokine 1999;11(10):729–35.
[6] Kharitonenkov A, Shiyanova TL, Koester A, et al. FGF-21 as a novel metabolic regulator. J Clin Invest 2005;115(6):1627–35.
[7] Badman MK, Pissios P, Kennedy AR, Koukos G, Flier JS, Maratos-Flier E. Hepatic fibroblast growth factor 21 is regulated by PPARalpha and is a key mediator of hepatic lipid metabolism in ketotic states. Cell Metab 2007;5(6):426–37.
[8] BonDurant LD, Ameka M, Naber MC, et al. FGF21 regulates metabolism through adipose-dependent and -Independent mechanisms. Cell Metab 2017;25(4):935–44 e4.
[9] Soberg S, Sandholt CH, Jespersen NZ, et al. FGF21 is a sugar-induced hormone associated with sweet intake and preference in humans. Cell Metab 2017;25(5):1045–53 e6.
[10] Bookout AL, de Groot MH, Owen BM, et al. FGF21 regulates metabolism and circadian behavior by acting on the nervous system. Nat Med 2013;19(9):1147–52.
[11] Shimada T, Hasegawa H, Yamazaki Y, et al. FGF-23 is a potent regulator of vitamin D metabolism and phosphate homeostasis. J Bone Miner Res 2004;19(3):429–35.
[12] Shimada T, Kakitani M, Yamazaki Y, et al. Targeted ablation of FGF23 demonstrates an essential physiological role of FGF23 in phosphate and vitamin D metabolism. J Clin Invest 2004;113(4):561–8.
[13] Itoh N. Hormone-like (endocrine) FGFs: their evolutionary history and roles in development, metabolism, and disease. Cell Tissue Res 2010;342(1):1–11.
[14] Sarrazin S, Lamanna WC, Esko JD. Heparan sulfate proteoglycans. Cold Spring Harb Perspect Biol 2011;3(7).

[15] Perrimon N, Bernfield M. Specificities of heparan sulphate proteoglycans in developmental processes. Nature 2000;404(6779):725–8.
[16] Asada M, Shinomiya M, Suzuki M, et al. Glycosaminoglycan affinity of the complete fibroblast growth factor family. Biochim Biophys Acta 2009;1790(1):40–8.
[17] Goetz R, Beenken A, Ibrahimi OA, et al. Molecular insights into the klotho-dependent, endocrine mode of action of fibroblast growth factor 19 subfamily members. Mole and Cell Biol 2007;27(9):3417–28.
[18] Kuro-o M. Endocrine FGFs and Klothos: emerging concepts. Trends Endocrinol Metab 2008;19(7):239–45.
[19] Ito S, Fujimori T, Hayashizaki Y, Nabeshima Y. Identification of a novel mouse membrane-bound family 1 glycosidase-like protein, which carries an atypical active site structure. Biochim Biophys Acta 2002;1576(3):341–5.
[20] Kuro-o M, Matsumura Y, Aizawa H, et al. Mutation of the mouse klotho gene leads to a syndrome resembling ageing. Nature 1997;390(6655):45–51.
[21] Kurosu H, Ogawa Y, Miyoshi M, et al. Regulation of fibroblast growth factor-23 signaling by klotho. J Biol Chem 2006;281(10):6120–3.
[22] Ding X, Boney-Montoya J, Owen BM, et al. betaKlotho is required for fibroblast growth factor 21 effects on growth and metabolism. Cell Metab 2012;16(3):387–93.
[23] Kurosu H, Choi M, Ogawa Y, et al. Tissue-specific expression of betaKlotho and fibroblast growth factor (FGF) receptor isoforms determines metabolic activity of FGF19 and FGF21. J Biol Chem 2007;282(37):26687–95.
[24] Li SA, Watanabe M, Yamada H, Nagai A, Kinuta M, Takei K. Immunohistochemical localization of Klotho protein in brain, kidney, and reproductive organs of mice. Cell Struct Funct 2004;29(4):91–9.
[25] Urakawa I, Yamazaki Y, Shimada T, et al. Klotho converts canonical FGF receptor into a specific receptor for FGF23. Nature 2006;444(7120):770–4.
[26] Ito S, Kinoshita S, Shiraishi N, et al. Molecular cloning and expression analyses of mouse betaklotho, which encodes a novel Klotho family protein. Mech Dev 2000;98(1–2):115–19.
[27] Chen G, Liu Y, Goetz R, et al. alpha-Klotho is a non-enzymatic molecular scaffold for FGF23 hormone signalling. Nature 2018;553(7689):461–6.
[28] Lee S, Choi J, Mohanty J, et al. Structures of beta-klotho reveal a 'zip code'-like mechanism for endocrine FGF signalling. Nature 2018;553(7689):501–5.
[29] Markan KR, Potthoff MJ. Metabolic fibroblast growth factors (FGFs): mediators of energy homeostasis. Semin Cell Dev Biol 2016;53:85–93.
[30] Mohammadi M, Olsen SK, Ibrahimi OA. Structural basis for fibroblast growth factor receptor activation. Cytokine Growth Factor Rev 2005;16(2):107–37.
[31] Ibrahimi OA, Zhang F, Eliseenkova AV, Itoh N, Linhardt RJ, Mohammadi M. Biochemical analysis of pathogenic ligand-dependent FGFR2 mutations suggests distinct pathophysiological mechanisms for craniofacial and limb abnormalities. Hum Mol Genet 2004;13(19):2313–24.
[32] Song L, Zhu Y, Wang H, et al. A solid-phase PEGylation strategy for protein therapeutics using a potent FGF21 analog. Biomaterials 2014;35(19):5206–15.
[33] Huang J, Ishino T, Chen G, et al. Development of a novel long-acting antidiabetic FGF21 mimetic by targeted conjugation to a scaffold antibody. J Pharmacol Exp Ther 2013;346(2):270–80.
[34] Mu J, Pinkstaff J, Li Z, et al. FGF21 analogs of sustained action enabled by orthogonal biosynthesis demonstrate enhanced antidiabetic pharmacology in rodents. Diabetes 2012;61(2):505–12.
[35] Min X, Weiszmann J, Johnstone S, et al. Agonistic beta-Klotho antibody mimics fibroblast growth factor 21 (FGF21) functions. J Biol Chem 2018;293(38):14678–88.
[36] Agrawal A, Parlee S, Perez-Tilve D, et al. Molecular elements in FGF19 and FGF21 defining KLB/FGFR activity and specificity. Mol Metab 2018;13:45–55.
[37] Huang Z, Tan Y, Gu J, et al. Uncoupling the mitogenic and metabolic functions of FGF1 by tuning FGF1-FGF receptor dimer stability. Cell Rep 2017;20(7):1717–28.
[38] Schlessinger J, Plotnikov AN, Ibrahimi OA, et al. Crystal structure of a ternary FGF-FGFR-heparin complex reveals a dual role for heparin in FGFR binding and dimerization. Mol Cell 2000;6(3):743–50.
[39] Luo Y, Lu W, Mohamedali KA, et al. The glycine box: a determinant of specificity for fibroblast growth factor. Biochemistry 1998;37(47):16506–15.
[40] Beenken A, Mohammadi M. The structural biology of the FGF19 subfamily. Adv Exp Med Biol 2012;728:1–24.
[41] Wu X, Ge H, Gupte J, et al. Co-receptor requirements for fibroblast growth factor-19 signaling. J Biol Chem 2007;282(40):29069–72.
[42] Kharitonenkov A, Dunbar JD, Bina HA, et al. FGF-21/FGF-21 receptor interaction and activation is determined by betaKlotho. J Cell Physiol 2008;215(1):1–7.
[43] Suzuki M, Uehara Y, Motomura-Matsuzaka K, et al. beta Klotho is required for fibroblast growth factor (FGF) 21 signaling through FGF receptor (FGFR) 1c and FGFR3c. Mol Endocrinol 2008;22(4):1006–14.
[44] Xu J, Lloyd DJ, Hale C, et al. Fibroblast growth factor 21 reverses hepatic steatosis, increases energy expenditure, and improves insulin sensitivity in diet-induced obese mice. Diabetes 2009;58(1):250–9.
[45] Suh JM, Jonker JW, Ahmadian M, et al. Endocrinization of FGF1 produces a neomorphic and potent insulin sensitizer. Nature 2014;513(7518):436–9.
[46] Apweiler R, Freund P. Development of glucose intolerance in obese (fa/fa) Zucker rats. Horm Metab Res 1993;25(10):521–4.
[47] Lewis GF. Lipid metabolism. Curr Opin Lipidol 2002;13(1):97–9.
[48] Zhou QL, Jiang ZY, Holik J, et al. Akt substrate TBC1D1 regulates GLUT1 expression through the mTOR pathway in 3T3-L1 adipocytes. Biochem J 2008;411(3):647–55.
[49] Nishimura H, Simpson IA. Staurosporine inhibits phorbol 12-myristate 13-acetate- and insulin-stimulated translocation of GLUT1 and GLUT4 glucose transporters in rat adipose cells. Biochem J 1994;302(Pt 1):271–7.
[50] Yang J, Holman GD. Comparison of GLUT4 and GLUT1 subcellular trafficking in basal and insulin-stimulated 3T3-L1 cells. J Biol Chem 1993;268(7):4600–3.
[51] Fisher FM, Kleiner S, Douris N, et al. FGF21 regulates PGC-1alpha and browning of white adipose tissues in adaptive thermogenesis. Genes Dev 2012;26(3):271–81.
[52] Tanaka Y, Ohto H, Kohno M, Cho F, Honjo S. [Spontaneous diabetes mellitus in cynomolgus monkeys (Macaca fascicularis)]. Jikken Dobutsu 1986;35(1):11–19.
[53] Yasuda M, Takaoka M, Fujiwara T, Mori M. Occurrence of spontaneous diabetes mellitus in a cynomolgus monkey (Macaca fascicularis) and impaired glucose tolerance in its descendants. J Med Primatol 1988;17(6):319–32.
[54] Wagner JD, Shadoan MK, Zhang L, et al. A selective peroxisome proliferator-activated receptor alpha agonist, CP-900691, improves plasma lipids, lipoproteins, and glycemic control in diabetic monkeys. J Pharmacol Exp Ther 2010;333(3):844–53.
[55] Tigno XT, Gerzanich G, Hansen BC. Age-related changes in metabolic parameters of nonhuman primates. J Gerontol A Biol Sci Med Sci 2004;59(11):1081–8.
[56] Koyama H, Tachibana Y, Takaura K, et al. Effects of housing conditions on behaviors and biochemical parameters in juvenile cynomolgus monkeys (Macaca fascicularis). Exp Anim 2019;68(2):195–211.
[57] Li H, Zhang J, Jia W. Fibroblast growth factor 21: a novel metabolic regulator from pharmacology to physiology. Front Med 2013;7(1):25–30.
[58] Gaich G, Chien JY, Fu H, et al. The effects of LY2405319, an FGF21 analog, in obese human subjects with type 2 diabetes. Cell Metab 2013;18(3):333–40.
[59] Foltz IN, Hu S, King C, et al. Treating diabetes and obesity with an FGF21-mimetic antibody activating the betaKlotho/FGFR1c receptor complex. Sci Transl Med 2012;4(162) 162ra53.
[60] Stanislaus S, Hecht R, Yie J, et al. A novel Fc-FGF21 with improved resistance to proteolysis, increased affinity toward beta-Klotho, and enhanced efficacy in mice and cynomolgus monkeys. Endocrinology 2017;158(5):1314–27.
[61] Veniant MM, Komorowski R, Chen P, et al. Long-acting FGF21 has enhanced efficacy in diet-induced obese mice and in obese rhesus monkeys. Endocrinology 2012;153(9):4192–203.
[62] Talukdar S, Zhou Y, Li D, et al. A long-acting FGF21 molecule, PF-05231023, decreases body weight and improves lipid profile in non-human primates and type 2 diabetic subjects. Cell Metab 2016;23(3):427–40.
[63] Bagdade JD, Wagner JD, Rudel LL, Clarkson TB. Accelerated cholesteryl ester transfer and altered lipoprotein composition in diabetic cynomolgus monkeys. J Lipid Res 1995;36(4):759–66.
[64] Wagner JD, Cline JM, Shadoan MK, Bullock BC, Rankin SE, Cefalu WT. Naturally occurring and experimental diabetes in cynomolgus monkeys: a comparison of carbohydrate and lipid metabolism and islet pathology. Toxicol Pathol 2001;29(1):142–8.
[65] Bauer SA, Arndt TP, Leslie KE, Pearl DL, Turner PV. Obesity in rhesus and cynomolgus macaques: a comparative review of the condition and its implications for research. Comp Med 2011;61(6):514–26.
[66] Sherman MR, Williams LD, Sobczyk MA, Michaels SJ, Saifer MG. Role of the methoxy group in immune responses to mPEG-protein conjugates. Bioconjug Chem 2012;23(3):485–99.
[67] Saifer MG, Williams LD, Sobczyk MA, Michaels SJ, Sherman MR. Selectivity of binding of PEGs and PEG-like oligomers to anti-PEG antibodies induced by methoxyPEG-proteins. Mol Immunol 2014;57(2):236–46.